The Barrier Layer Effect on the Heat and Freshwater Balance from Moored Observations in the Eastern Pacific Fresh Pool

SHOTA KATSURA,[a] JANET SPRINTALL,[a] J. THOMAS FARRAR,[b] DONGXIAO ZHANG,[c,d] AND MEGHAN F. CRONIN[d]

[a] *Scripps Institution of Oceanography, University of California, San Diego, La Jolla, California*
[b] *Department of Physical Oceanography, Woods Hole Oceanographic Institution, Woods Hole, Massachusetts*
[c] *Cooperative Institute for Climate, Ocean, and Ecosystem Studies, University of Washington, Seattle, Washington*
[d] *NOAA/Pacific Marine Environmental Laboratory, Seattle, Washington*

(Manuscript received 4 November 2021, in final form 4 March 2022)

ABSTRACT: Formation and evolution of barrier layers (BLs) and associated temperature inversions (TIs) were investigated using a 1-yr time series of oceanic and air–sea surface observations from three moorings deployed in the eastern Pacific fresh pool. BL thickness and TI amplitude showed a seasonality with maxima in boreal summer and autumn when BLs were persistently present. Mixed layer salinity (MLS) and mixed layer temperature (MLT) budgets were constructed to investigate the formation mechanism of BLs and TIs. The MLS budget showed that BLs were initially formed in response to horizontal advection of freshwater in boreal summer and then primarily maintained by precipitation. The MLT budget revealed that penetration of shortwave radiation through the mixed layer base is the dominant contributor to TI formation through subsurface warming. Geostrophic advection is a secondary contributor to TI formation through surface cooling. When the BL exists, the cooling effect from entrainment and the warming effect from detrainment are both significantly reduced. In addition, when the BL is associated with the presence of a TI, entrainment works to warm the mixed layer. The presence of BLs makes the shallower mixed layer more sensitive to surface heat and freshwater fluxes, acting to enhance the formation of TIs that increase the subsurface warming via shortwave penetration.

KEYWORDS: Ocean; North Pacific Ocean; Tropics; Entrainment; Oceanic mixed layer; Salinity

1. Introduction

Temperature, salinity, and density of seawater are typically vertically uniform from the sea surface to the maximum depth of convective overturning, referred to as the mixed layer depth. Exchanges of heat, freshwater, and momentum occur in the surface mixed layer at the interface of the atmosphere and ocean. The depth of the mixed layer determines the heat and freshwater content of the upper ocean and its sensitivity to atmospheric forcing. Since the mixed layer temperature (MLT) and salinity (MLS) are almost the same as the sea surface temperature (SST) and salinity (SSS), respectively, knowledge of the heat and freshwater balance within the mixed layer is important to better understand heat and freshwater exchange between the atmosphere and the ocean. Hence, the budget analysis of the MLT (e.g., Foltz et al. 2003; Foltz and McPhaden 2005; Wijesekera et al. 2005; Dong et al. 2007; Girishkumar et al. 2017) and MLS (e.g., Foltz et al. 2004; Wijesekera et al. 2005; Ren and Riser 2009; Bingham et al. 2010; Ren et al. 2011; Katsura et al. 2013) have been undertaken in many different regions of the global ocean to study climate variability, air–sea interaction, and the hydrological cycle.

While the density-defined mixed layer depth (MLD) generally agrees well with the temperature-defined isothermal layer depth (ILD), a mismatch is known to exist in some regions (e.g., Sprintall and Tomczak 1992; de Boyer Montégut et al. 2007). In the case where the mixed layer depth is shallower than the isothermal layer depth due to salinity stratification, the region between these depths is called a barrier layer (BL; Godfrey and Lindstrom 1989; Lukas and Lindstrom 1991). The name BL is derived from its potential role as a barrier against the vertical exchange of heat and momentum between the sea surface and the subsurface. When a BL exists, the cooling of the surface mixed layer through entrainment of the cooler water from below the mixed layer and vertical diffusion at the mixed layer base is potentially reduced because the temperature within the BL is almost the same as the overlying mixed layer. Temperature inversions (TIs), a layer where temperature increases with depth, are frequently found within BLs, but the fresher stratification associated with the BLs compensates for any potential density instability due to the TI (Katsura and Sprintall 2020, hereafter KS2020). When a BL is associated with a TI, the effect of entrainment and vertical diffusion can lead to warming within the mixed layer. Since BLs tend to be associated with a shallow mixed layer, the existence of the salinity-stratified BL can make the mixed layer more sensitive to surface heat, freshwater, and momentum flux and modify the MLT and MLS balance. Indeed, BLs can cause the acceleration of surface flow by trapping the momentum flux from the wind within the shallow mixed layer above the BL (Roemmich et al. 1994; Vialard and Delecluse 1998a; Cronin and McPhaden 2002). For all these reasons, BLs are thought to play an important role in air–sea interaction and climate variability (e.g., Vialard and Delecluse 1998b; Masson et al. 2004; Balaguru et al. 2012).

In the eastern tropical North Pacific, BLs are distributed along the SSS front on the southern border of the eastern Pacific fresh pool (EPFP). The seasonal maximum of the BL in this region occurs in boreal summer and autumn with a typical

---

Corresponding author: Shota Katsura, skatsura@ucsd.edu

DOI: 10.1175/JPO-D-21-0243.1

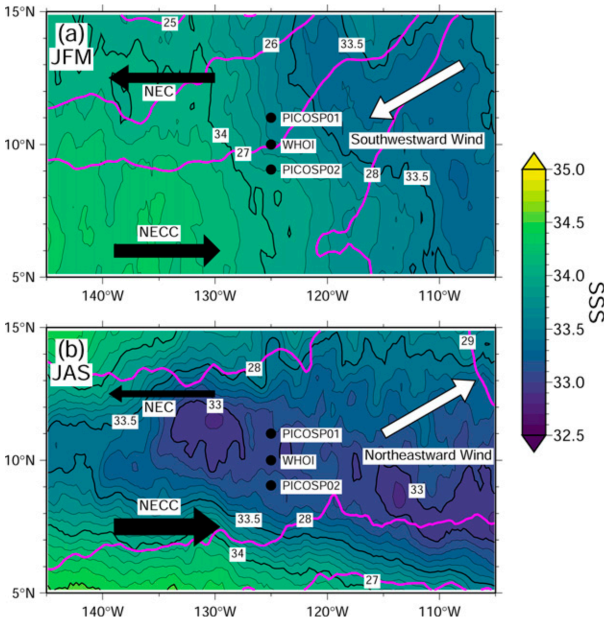

FIG. 1. Distribution of mean sea surface salinity from Soil Moisture Active Passive (SMAP) (black contours and color) and mean sea surface temperature from Optimum Interpolation Sea Surface Temperature (OISST) (magenta contours) averaged over (a) January–March and (b) July–September in 2016–17. Black circles indicate the location of the PICOSP01 (11°N, 125°W), WHOI (10°N, 125°W), and PICOSP02 (9.05°N, 125°W) moorings deployed as part of the SPURS-2 field campaign. The westward North Equatorial Current (NEC) and the eastward North Equatorial Countercurrent (NECC) are schematically indicated by black arrows. White arrows schematically indicate the southwestward wind in boreal winter in (a) and the northeastward wind in boreal summer in (b) over the SPURS-2 mooring sites.

thickness of 20–30 m (KS2020). In boreal autumn, BLs in this region tend to be associated with TIs. Southward Ekman advection driven by eastward wind was a prime contributor to climatological BL and TI formation causing both freshening and cooling of the surface layer through the tilting of the SSS front (KS2020). Considering the extremely shallow mixed layer above BLs in the eastern tropical North Pacific (typically 30 m; Suga et al. 2004; KS2020), BLs in this region potentially have a significant impact on the MLT budget and hence the SST variability compared to other regions where BLs are present.

A multiyear field program to study the upper-ocean salinity structure and the physical processes controlling the salinity balance, known as the Salinity Processes in the Upper-Ocean Regional Study 2 (SPURS-2), was conducted in the eastern tropical Pacific (Lindstrom et al. 2019). The focal site of the SPURS-2 field program was around 10°N, 125°W in the western part of the EPFP (Fig. 1). The EPFP is a relatively homogenous pool of low mean SSS (<34.0) resulting from the high precipitation that varies seasonally due to the meridional shift in the intertropical convergence zone (ITCZ; Fig. 1). The semisynoptic shipboard measurements undertaken during two SPURS-2 cruises in 2016 and 2017 showed that BLs within the EPFP were associated with surface freshening both by precipitation and Ekman advection (Katsura et al. 2021). The transition zone between the EPFP and the SSS front was a critical region for BL and TI formation through the tilting of the SSS front with geostrophic advection playing a dominant role in this process (Katsura et al. 2021). However, the formation of BLs and TIs during the two cruises suggested a relatively patchy distribution that can potentially reduce the effectiveness of the BL impact on heat exchange through entrainment or through air–sea interaction. Nonetheless, the cruise data were too limited in time and space to determine the persistence of BLs and TIs, much less to examine their role in the MLS and MLT budgets.

The overarching goal of this study is to investigate the impact of the presence of BLs and TIs in the EPFP on the MLT and MLS balance. During the SPURS-2 field campaign, three moorings were deployed within the EPFP (Fig. 1), and each recorded time series of the temperature and salinity profiles for about one year. The year-long time series of daily mooring observations enable the determination of more detailed characteristics of the BLs and TIs within the EPFP such as their formation, persistence, and decay and their influence on the MLS and MLT budgets. Moreover, the spatially fixed time series from the mooring allows us to evaluate the impact of the BL on the entrainment cooling and the sensitivity of the mixed layer to the surface flux, something that was not possible with data from Argo profiling floats (KS2020) or from the synoptic SPURS-2 shipboard surveys (Katsura et al. 2021).

2. Data and methods

a. Data

Our analysis used the upper-ocean profile time series from three moorings deployed in the eastern tropical North Pacific as a part of the SPURS-2 field campaign: the mooring deployed by Woods Hole Oceanographic Institution at 10°N, 125°W (henceforth WHOI mooring; Farrar and Plueddemann 2019) and two moorings deployed by the NOAA Pacific Marine Environmental Laboratory at 11°N, 125°W (henceforth PICOSP01 mooring) and at 9.05°N, 125°W (henceforth PICOSP02 mooring; Fig. 1).

The WHOI mooring measured temperature and salinity using discrete instrument sampling at ~5-min intervals from 24 August 2016 to 6 November 2017 (Farrar and Plueddemann 2019). The vertical spacing between each sensor was ~3 m from 1 to 25 m and ~5 m from 25 to 101 m. Temperature and salinity profiles at the WHOI mooring were vertically interpolated into a 1-dbar interval using an Akima spline (Akima 1970). Potential temperature (θ) and density (σ_θ) were calculated after the vertical interpolation, and then all profiles were daily averaged. Horizontal currents were measured using a series of both discrete current meters and acoustic Doppler current profilers (ADCPs) strung along the mooring line. The current profile between 3 and 285 m was interpolated from the sensors into 1-m and 1-hourly bins.

Time series from the PICOSP01 and PICOSP02 moorings extended from 25 August 2016 to 3 July 2017 and from 22 August

2016 to 2 November 2017, respectively. These moorings used Profiling Crawler (PRAWLER) technology (Osse et al. 2015), which are essentially small, low-cost moored buoys equipped with a CTD that is powered by waves to move up and down the mooring line, thus creating temperature and salinity profiles of the upper ocean. The CTD on the PICOSP02 mooring operated for 14 months with small gaps in the time series on 24–25 and 29 September 2016, while the CTD on the PICOSP01 mooring failed in July 2017 after 10 months operation. The PICOSP01 and PICOSP02 moorings both measured temperature and salinity profiles approximately every 3 h from ~5 to 455 m (with PICOSP01 between 5 and 362 m during the two months of November and December), at vertical intervals of ~1 m above 30 m and ~2 m below 30 m. Like the WHOI mooring data, θ and σ_θ were calculated, and the profiles of salinity, θ, and σ_θ were daily averaged. The PICOSP moorings did not include an ADCP.

All three moored buoys measured wind, air temperature and humidity, which can be used to estimate the surface wind stress, sensible and latent heat flux. The WHOI mooring also measured the evaporation and precipitation as well as the downward shortwave and longwave radiation, making it possible to estimate the net surface heat flux. For the WHOI mooring, the turbulent sensible and latent heat fluxes were computed using the COARE 3.5 algorithm (Fairall et al. 2003; Edson et al. 2013) using the measured SST [extrapolated to the air–sea interface using the Fairall et al. (1996) warm layer and cool-skin corrections], air temperature, relative humidity, wind, and surface current speed and direction, downwelling solar and longwave radiometers, and surface air pressure. Due to the failure of the relative humidity sensor at the PICOSP02 mooring, turbulent fluxes on that mooring could not be computed after 22 October 2016.

Comparison of wind stress at the WHOI and PICOSP moorings, calculated using the COARE 3.5 algorithm, found the wind stress at the PICOSP moorings had smaller amplitudes compared to the WHOI mooring. One possible reason could be that the wind sensors on the PICOSP moorings were too low (~1 m above water line), and thus within the wave boundary layer. Hence wind stress and Ekman transport estimated using the PICOSP mooring data were deemed unreliable. Instead, for the PICOSP moorings, we used the Cross-Calibrated Multi-Platform (CCMP) wind product (see below). To calculate relative wind stress to the ocean, we used the COARE algorithm and the current from 3 m at the WHOI mooring. The Ocean Surface Current Analyses Real-Time (OSCAR; Bonjean and Lagerloef 2002; Johnson et al. 2007) product was also used to compute Ekman flow as described in section 2c. The relative wind stress measured at the WHOI mooring along with the heat flux estimated at the WHOI and PICOSP moorings were all daily averaged.

Precipitation at the WHOI and PICOSP01 moorings was measured for the entire time period of deployment. At the PICOSP02 mooring, precipitation was measured from 22 August 2016 to 24 October 2017, which was 9 days shorter than the observation period of temperature and salinity profiles. To fill this gap of precipitation at the PICOSP02 mooring, the NASA Integrated Multi-satellitE Retrievals for GPM (IMERG) version 4.0 was used, which is a merged satellite precipitation product available from 2014 every 30 min at 0.1° latitude × 0.1° longitude horizontal resolution (Kummerow 1998). The IMERG precipitation and the rainfall observations at the SPURS-2 moorings showed good agreement over the deployment period of each mooring although the rainfall observations at the SPURS-2 moorings tended to be slightly larger than IMERG (not shown).

Other data products used in the analysis are SSS from the daily L3 8-day running mean 70-km version 4.0 product of the National Aeronautics and Space Administration (NASA) Soil Moisture Active Passive (SMAP; Meissner and Wentz 2019), SST from the Advanced Very High Resolution Radiometer daily product of Optimum Interpolation Sea Surface Temperature (OISST; Reynolds et al. 2007), and daily sea surface height (SSH) from Copernicus Marine Environment Monitoring Service (CMEMS). The horizontal resolution of all these daily gridded data is 0.25° latitude × 0.25° longitude. The Cross-Calibrated Multi-Platform (CCMP) gridded surface vector winds version 2.0 (Wentz et al. 2015) was also used to calculate vertical velocity at the mixed layer base in appendix B. The CCMP wind product is gridded to 0.25° latitude × 0.25° longitude and 6 h. Wind stress at each grid point was estimated from the CCMP wind relative to the surface current at the WHOI mooring using the COARE 3.5 algorithm to compute the vertical velocity driven by the convergence and divergence of the effective wind stress in appendix B. The CCMP wind and wind stress showed a good agreement with those observed at the WHOI mooring in terms of phase, direction, and amplitude (not shown). The CCMP wind and wind stress were daily averaged. The OSCAR (Bonjean and Lagerloef 2002; Johnson et al. 2007) product was used to compute Ekman flow at the PICOSP moorings as described in section 2c. The OSCAR product is meant to represent the average current of the upper 30 m based on satellite observations with a horizontal resolution of 1/3° latitude × 1/3° longitude and a 5-day temporal interval. A good agreement was found between the OSCAR current and the observed near-surface current at the WHOI mooring in terms of phase, direction, and amplitude (not shown).

b. *Definition of BLs and TIs*

MLD, ILD, BL thickness (BLT), and the amplitude of the TI were calculated from the daily averaged profiles at each SPURS-2 mooring following KS2020 and Katsura et al. (2021). The ILD was defined as the depth at which potential temperature θ decreases by 0.2°C from 10-dbar depth (de Boyer Montégut et al. 2007). The MLD was defined as the depth at which potential density σ_θ increases from 10-dbar depth by the equivalent value to a temperature decrease of 0.2°C at 10-dbar salinity (Sprintall and Tomczak 1992). The BLT was defined as the difference between the ILD and MLD when that difference is greater than zero. For BLT > 10 dbar, the amplitude of any associated TI ($\Delta\theta$) was defined as the difference between the temperature at the vertical temperature maximum within the BL minus the temperature at the MLD (KS2020).

c. Mixed layer temperature and salinity budget

To evaluate the formation of BLs and TIs and their impact on air–sea interaction, MLS and MLT budgets were constructed. The derivation of the MLS and MLT budget equations starts with the approximate equations governing conservation of salt, heat, and mass (e.g., Moisan and Niiler 1998):

$$\frac{\partial S}{\partial t} + u\frac{\partial S}{\partial x} + v\frac{\partial S}{\partial y} + w\frac{\partial S}{\partial z} = -\frac{\partial \mathrm{FS}}{\partial z}, \tag{1}$$

$$\rho_0 c_p\left(\frac{\partial T}{\partial t} + u\frac{\partial T}{\partial x} + v\frac{\partial T}{\partial y} + w\frac{\partial T}{\partial z}\right) = \frac{\partial Q}{\partial z}, \quad \text{and} \tag{2}$$

$$\frac{\partial u}{\partial x} + \frac{\partial v}{\partial y} + \frac{\partial w}{\partial z} = 0, \tag{3}$$

where S is salinity, T is temperature, u is zonal velocity, v is meridional velocity, w is vertical velocity, F is the freshwater flux, ρ_0 is the reference density of seawater (1025 kg m^{-3}), c_p is the specific heat of seawater (3850 J kg^{-1} °C^{-1}), and Q is the heat flux. Combining Eqs. (1) and (2) with Eq. (3) and integrating each from the MLD ($z = -h_m$) to the sea surface ($z = 0$) and adding the contribution of vertical turbulence mixing, the MLS and MLT budget equations are derived as

$$\underbrace{\frac{\partial S_m}{\partial t}}_{1} = \underbrace{\frac{ES_0}{h_m}}_{2} - \underbrace{\frac{PS_0}{h_m}}_{3} - \underbrace{\mathbf{u}_m \cdot \nabla S_m}_{4} + \underbrace{S_{\mathrm{ent}}}_{5} + \underbrace{S_{\mathrm{turb}}}_{6} \\ - \underbrace{\frac{1}{h_m}\nabla \cdot \int_{-h_m}^{0} \hat{\mathbf{u}}\hat{S}\,dz}_{7}, \quad \text{and} \tag{4}$$

$$\underbrace{\frac{\partial T_m}{\partial t}}_{1} = \underbrace{\frac{Q_{\mathrm{net}}}{\rho_0 c_p h_m}}_{2} - \underbrace{\frac{Q_{\mathrm{pen}}}{\rho_0 c_p h_m}}_{3} - \underbrace{\mathbf{u}_m \cdot \nabla T_m}_{4} + \underbrace{T_{\mathrm{ent}}}_{5} + \underbrace{T_{\mathrm{turb}}}_{6} \\ - \underbrace{\frac{1}{h_m}\nabla \cdot \int_{-h_m}^{0} \hat{\mathbf{u}}\hat{\theta}\,dz}_{7}, \tag{5}$$

respectively (e.g., Moisan and Niiler 1998; Chi et al. 2021). Here, S_m is the MLS, E is evaporation, P is precipitation, S_0 is sea surface salinity, h_m is MLD, $\mathbf{u}_m$ is horizontal velocity averaged over the MLD, T_m is the MLT, Q_{net} is the net heat flux at the sea surface, Q_{pen} is the penetration of the downward shortwave radiation through the mixed layer base, S_{ent} and T_{ent} are the effect of entrainment/detrainment on the MLS and MLT budget, respectively, and S_{turb} and T_{turb} are the effect of vertical turbulence mixing at the base of the mixed layer on the MLS and MLT budget, respectively. For the derivation of the MLS budget equation (4), we used $F = P - E$ for $z = 0$ and $F = 0$ for $z \neq 0$. The “hats” indicate deviations from the vertical average, so that, e.g., $\theta(z) = \hat{\theta}(z) + T_m$. For Eq. (4), the left-hand side indicates the tendency of MLS (term 1), and the right-hand side represents the forcing terms: evaporation (term 2), precipitation (term 3), horizontal advection (term 4), entrainment (term 5), and vertical turbulent mixing (term 6). Similarly, for Eq. (5), the left-hand side indicates the tendency of MLT (term 1), and the right-hand side represents the forcing terms: net heat flux (term 2), shortwave penetration (term 3), horizontal advection (term 4), entrainment (term 5), and vertical turbulent mixing (term 6). For both Eqs. (4) and (5), there is a contribution from a term associated with the correlated vertical variations of temperature and velocity (term 7), which has the form of the divergence of a Reynolds correlation (or “eddy flux”). (Note, however, that term 7 is not an eddy flux in the conventional meaning of the term; that is, it is not associated with mesoscale or turbulent fluctuations, per se.)

Of the forcing terms in the MLS budget equation (4), precipitation (term 3) and horizontal advection (term 4) are possible contributors to BL formation through surface freshening (Figs. 2a,b; see also Cronin and McPhaden 2002). Precipitation (term 3) can form a fresh lens at the sea surface resulting in a BL formation (Fig. 2a). Evaporation (term 2) does not contribute to BL formation since it works to increase surface salinity and destabilize salinity stratification. Horizontal advection (term 4) can also contribute to BL formation by causing the surface freshening through the tilting of an SSS front when the velocity has a vertical shear within the isothermal layer (Fig. 2b). Similarly, among the forcing terms in the MLT budget equation (5), net heat flux (term 2), penetrative shortwave radiation (term 3), and horizontal advection (term 4) are possible factors of TI formation through net surface cooling (Figs. 2c,d). If net heat flux (term 2) is upward from the ocean to the atmosphere, it works to cool the surface layer and hence results in possible TI formation (Fig. 2c). The penetrative shortwave radiation (term 3) can contribute to TI formation when the magnitude of the penetrative warming below the mixed layer is larger than the MLT warming (term 1; Fig. 2c). Similar to the BL formation, the horizontal advection term (term 4) can also contribute to TI formation through surface cooling and/or the tilting of an isothermal surface where the resulting thermal destabilization is compensated by salinity stabilization (Fig. 2d). Since entrainment processes [term 5 in Eqs. (4) and (5)] and vertical turbulent mixing [term 6 in Eqs. (4) and (5)] work to destabilize the salinity stratification below the base of mixed layer and homogenize the vertical salinity and temperature profile, these terms do not contribute to either BL or TI formation.

The T_m and S_m were calculated as

$$T_m = \frac{1}{h_m}\int_{-h_m}^{0} \theta\,dz, \quad \text{and} \tag{6}$$

$$S_m = \frac{1}{h_m}\int_{-h_m}^{0} S\,dz, \tag{7}$$

respectively.

The net surface het flux (Q_{net}) was calculated as

$$Q_{\mathrm{net}} = Q_{\mathrm{SW}} + Q_{\mathrm{LW}} + Q_{\mathrm{LH}} + Q_{\mathrm{SH}}, \tag{8}$$

where Q_{SW} is the shortwave heat flux, Q_{LW} is the longwave heat flux, Q_{LH} is the latent heat flux, and Q_{SH} is the sensible

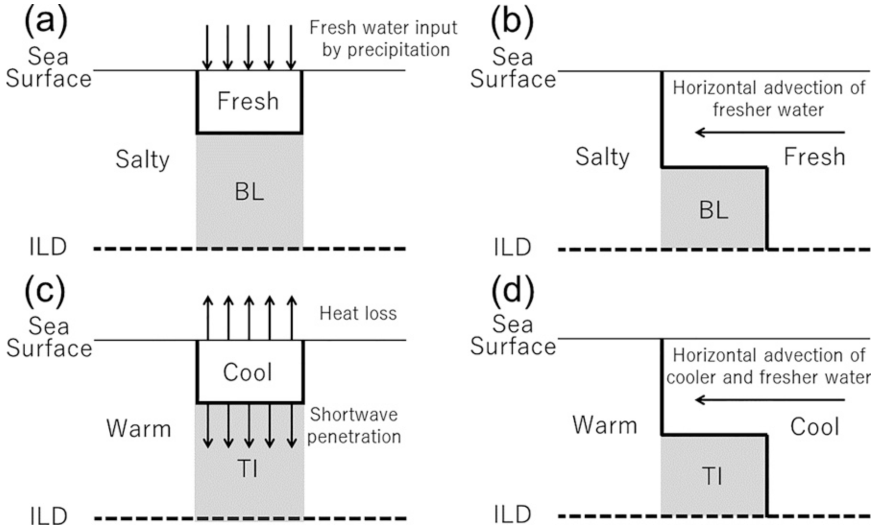

FIG. 2. Schematics of BL formation by (a) precipitation [term 3 in Eq. (4)] and (b) horizontal advection [term 4 in Eq. (4)] and TI formation by (c) net heat loss at the sea surface [term 2 in Eq. (5)] and shortwave penetration through the mixed layer base [term 3 in Eq. (5)] and (d) horizontal advection [term 4 in Eqs. (4) and (5)]. Gray shading indicates the resulting BL in (a) and (b) and the resulting TI (c) and (d). The thick line indicates the boundary between the salty and freshwater in (a) and (b) and the warm and cool water in (c) and (d). The thick dashed line indicates the ILD. After Cronin and McPhaden (2002).

heat flux (downward positive into the ocean). The penetrative radiation $Q_{\rm pen}$ was calculated using (Paulson and Simpson 1977):

$$Q_{\rm pen} = Q_{\rm SW}\left[R\exp\frac{-h_m}{\gamma_1} + (1-R)\exp\frac{-h_m}{\gamma_2}\right], \qquad (9)$$

where R is a separation constant ($=0.58$), and γ_1 ($=0.35$ m) and γ_2 ($=23.0$ m) are attenuation length scales (Jerlov 1976). As noted above, for the PICOSP moorings, the shortwave and longwave heat flux were not directly measured, so the values of $Q_{\rm SW}$ and $Q_{\rm LW}$ from the WHOI mooring were used. When $Q_{\rm LH}$ and $Q_{\rm SH}$ were not available at the PICOSP02 moorings after 22 October 2016 we filled the temporal gaps with values from the WHOI mooring.

The horizontal velocity ($\mathbf{u}_m$) in the horizontal advection term [term 4 in Eqs. (4) and (5)] was decomposed into Ekman and geostrophic components,

$$\mathbf{u}_m = \mathbf{u}_{\rm Ek} + \mathbf{u}_g, \qquad (10)$$

where $\mathbf{u}_{\rm Ek}$ is Ekman velocity and $\mathbf{u}_g$ is geostrophic velocity. For the WHOI mooring, the $\mathbf{u}_{\rm Ek}$ was calculated as

$$\mathbf{u}_{\rm Ek} = (u_{\rm Ek}, v_{\rm Ek}) = \frac{1}{\rho_0 f h_m}(\tau^y_{\rm eff}, -\tau^x_{\rm eff}), \qquad (11)$$

where, f is the Coriolis parameter, and $\tau^x_{\rm eff}$ and $\tau^y_{\rm eff}$ are the zonal and meridional effective wind stress, respectively. The effective wind stress $\boldsymbol{\tau}_{\rm eff} = (\tau^x_{\rm eff}, \tau^y_{\rm eff})$ is

$$\boldsymbol{\tau}_{\rm eff} = \boldsymbol{\tau}_0 - \boldsymbol{\tau}_p, \qquad (12)$$

where $\boldsymbol{\tau}_0$ is the wind stress and $\boldsymbol{\tau}_p$ is the stress associated with the pressure gradient-induced geostrophic shear (Cronin and Kessler 2009; Cronin and Tozuka 2016). (In this sense, $\mathbf{u}_{\rm Ek}$ includes components of both the conventional wind-driven "Ekman" flow and the geostrophic shear flow. Hence, to distinguish $\mathbf{u}_{\rm Ek}$ from the geostrophic velocity $\mathbf{u}_g$, we call $\mathbf{u}_{\rm Ek}$ the "Ekman velocity" and refer to $-\mathbf{u}_{\rm Ek}\cdot\nabla S_m$ as the "Ekman advection term" throughout this study.) The $\boldsymbol{\tau}_p$ was calculated as

$$\boldsymbol{\tau}_p = \frac{g\nu}{f}\left(\frac{\partial\rho}{\partial y}, -\frac{\partial\rho}{\partial x}\right) \qquad (13)$$

where g is the gravity constant, ν is the eddy viscosity, and ρ is the seawater density at the sea surface estimated using SSS from SMAP and SST from OISST. The eddy viscosity was calculated as

$$\nu = \frac{\boldsymbol{\tau}_0}{\rho_0\left(\dfrac{\partial\mathbf{u}}{\partial z}\right)} \qquad (14)$$

where $\mathbf{u}$ is the current velocity measured at the WHOI mooring. In the end, however, the magnitude of $\boldsymbol{\tau}_p$ at the SPURS-2 moorings was an order of magnitude smaller compared to the wind stress $\boldsymbol{\tau}_0$ (e.g., at the WHOI mooring, the mean magnitude of $\boldsymbol{\tau}_p = 0.93\times10^{-2}$ N m^{-2} compared to the mean magnitude of $\boldsymbol{\tau}_0 = 6.71\times10^{-2}$ N m^{-2}) since the SPURS-2 moorings were located within the EPFP where the horizontal gradient of density was small (Fig. 1).

The $\mathbf{u}_g$ at the WHOI mooring was calculated as the residual velocity ($\mathbf{u}_g = \mathbf{u}_m - \mathbf{u}_{\rm Ek}$), where $\mathbf{u}_m$ is estimated as the vertically averaged ADCP total current velocity within the mixed layer and $\mathbf{u}_{\mathrm{Ek}}$ given by Eq. (11). For the PICOSP moorings, the $\mathbf{u}_{\mathrm{Ek}}$ was computed as the OSCAR current minus $\mathbf{u}_g$ estimated from the SSH gradient. The horizontal gradients of MLS (∇S_m) and MLT (∇T_m) in the calculation of the horizontal advection term in Eqs. (4) and (5) were obtained from the gridded SSS from SMAP and SST from OISST, respectively. The values of SSS and SST were smoothed by taking the average of the grid points within a 2.5° radius of the mooring locations using a weighting function d^{-2}, where d is the distance in degrees. By using the horizontally smoothed SSS and SST fields for ∇S_m and ∇T_m, our calculation of the horizontal advection term lacks the eddy component. That is, when the horizontal advection term in Eq. (4) is expanded as

$$\mathbf{u}_m \cdot \nabla S_m = \mathbf{u}_m \cdot \nabla(\overline{S_m} + S'_m), \tag{15}$$

where the overbar indicates the long-term mean and the prime indicates the anomaly from the long-term mean (eddy component), our estimation corresponds to the first term on the right-hand side of Eq. (15) (mean component) and does not include the second term (eddy component). Thus, the second term on the right-hand side of Eq. (15) is a part of the unresolved residual of the MLS and MLT budget [Eqs. (4) and (5)] that will be pursued in appendix B.

For the estimation of the effect of the vertical turbulent mixing S_{turb} and T_{turb}, we assumed that these terms are driven by vertical diffusion and applied the following parameterization,

$$S_{\mathrm{turb}} = -\frac{\kappa_v}{h_m}\left(\frac{\partial S}{\partial z}\right), \quad \text{and} \tag{16}$$

$$T_{\mathrm{turb}} = -\frac{\kappa_v}{h_m}\left(\frac{\partial \theta}{\partial z}\right), \tag{17}$$

respectively, where κ_v is the vertical diffusivity. The vertical differentiation of temperature ($\partial\theta/\partial z$) and salinity ($\partial S/\partial z$) was calculated using the least squares method in the range between MLD and MLD + 5 dbar. We used a constant vertical diffusivity κ_v of 2×10^{-5} $\mathrm{m^2\ s^{-1}}$ (Farrar and Plueddemann 2019).

The full form of the entrainment terms S_{ent} and T_{ent} is

$$S_{\mathrm{ent}} = \left(\underbrace{\frac{\partial h_m}{\partial t}}_{1} + \underbrace{\mathbf{u}_{-h} \cdot \nabla h_m}_{2} + \underbrace{w_{-h}}_{3}\right)\frac{(S_m - S_{-h})}{h_m}, \quad \text{and} \tag{18}$$

$$T_{\mathrm{ent}} = \left(\underbrace{\frac{\partial h_m}{\partial t}}_{1} + \underbrace{\mathbf{u}_{-h} \cdot \nabla h_m}_{2} + \underbrace{w_{-h}}_{3}\right)\frac{(T_m - T_{-h})}{h_m}, \tag{19}$$

where $\mathbf{u}_{-h}$ and w_{-h} are the horizontal and vertical velocity at the base of the mixed layer, respectively, and S_{-h} and T_{-h} are the salinity and temperature at the MLD, respectively. The entrainment term [Eqs. (18) and (19)] consists of the effect of change of the MLD (term 1), lateral induction (term 2), and vertical advection across the mixed layer base (term 3).

Because the vertical velocity at the mixed layer base (w_{-h}) and the horizontal gradients of MLD (∇h_m) are difficult to observe, many studies estimate only the $\partial h_m/\partial t$ term [term 1 in Eqs. (18) and (19)] and call this the "entrainment term," lumping the neglected terms into the residual (e.g., Cronin et al. 2013; Farrar et al. 2015; Farrar and Plueddemann 2019). Here, we will also use this truncated form of the entrainment term, but we will attempt an estimate of the term related to the vertical velocity term w_{-h} (appendix B).

To estimate the entrainment term [term 1 in Eqs. (18) and (19)], we applied an explicit formulation following Kim et al. (2006). In the case of entrainment associated with the deepening of the mixed layer from $h_m(t)$ to $h_m(t + \Delta t)$ during Δt [where $h_m(t + \Delta t) > h_m(t)$], we write

$$T_m(t)h_m(t) + \int_{-h_m(t+\Delta t)}^{-h_m(t)} \theta(z)dz = T_m(t + \Delta t)h_m(t + \Delta t) \tag{20}$$

based on the conservation of the heat quantity without any other forcing. Here, the left-hand and right-hand sides of Eq. (20) indicate the heat quantity of the water column from the sea surface to $h_m(t + \Delta t)$ before and after deepening, respectively. Equation (20) also works for the case of detrainment associated with the shoaling of the mixed layer; in that case the second term is subtracted, and the integral limits are from $h_m(t)$ to $h_m(t + \Delta t)$ during Δt [where $h_m(t + \Delta t) < h_m(t)$]. Equation (20) can be transformed to

$$\begin{aligned} T_{\mathrm{ent}} &= \frac{T_m(t + \Delta t) - T_m(t)}{\Delta t} \\ &= \frac{1}{\Delta t}\left[\frac{1}{h_m(t + \Delta t)}\int_{-h_m(t+\Delta t)}^{-h_m(t)} \theta(z)dz - DT_m(t)\right], \end{aligned} \tag{21}$$

where $\Delta t = 1$ day, and D is the deepening rate,

$$D = \frac{h_m(t + \Delta t) - h_m(t)}{h_m(t + \Delta t)}. \tag{22}$$

Positive and negative D indicates the deepening (entrainment) and shoaling (detrainment) of the mixed layer, respectively. The term S_{ent} can be written in the same way,

$$S_{\mathrm{ent}} = \frac{1}{\Delta t}\left[\frac{1}{h_m(t + \Delta t)}\int_{-h_m(t+\Delta t)}^{-h_m(t)} S(z)dz - DS_m(t)\right]. \tag{23}$$

The calculation of entrainment terms using Eqs. (21) and (23) is simply a finite-difference approximation to Eqs. (18) and (19), neglecting the effect of lateral induction (term 2) and vertical advection (term 3). The advantage of this calculation is the ability to explicitly evaluate the effect of BLs and TIs on the entrainment term.

In this study, the eddy flux (term 7) in Eqs. (4) and (5) was treated as a residual of the MLS and MLT budget because it cannot be accurately estimated without the horizontal distribution of the vertical profile of horizontal velocity (i.e., $\nabla \cdot \int_{-h_m}^{0} \hat{\mathbf{u}}\hat{\theta}\,dz$ and $\nabla \cdot \int_{-h_m}^{0} \hat{\mathbf{u}}\hat{S}\,dz$). Hence, the final form of the MLS and MLT budget equations used in this study are

$$\frac{\partial S_m}{\partial t} = \frac{ES_0}{h_m} - \frac{PS_0}{h_m} - \mathbf{u}_{\mathrm{Ek}} \cdot \nabla S_m - \mathbf{u}_g \cdot \nabla S_m - \frac{\kappa_v}{h_m}\left(\frac{\partial S}{\partial z}\right) + S_{\mathrm{ent}} + R_S, \quad \text{and} \tag{24}$$

$$\frac{\partial T_m}{\partial t} = \frac{Q_{\mathrm{net}}}{\rho_0 c_p h_m} - \frac{Q_{\mathrm{pen}}}{\rho_0 c_p h_m} - \mathbf{u}_{\mathrm{Ek}} \cdot \nabla T_m - \mathbf{u}_g \cdot \nabla T_m - \frac{\kappa_v}{h_m}\left(\frac{\partial T}{\partial z}\right) + T_{\mathrm{ent}} + R_T, \tag{25}$$

respectively. Here, R_S and R_T are the residual of the MLS and MLT budget, respectively. Each term in Eqs. (24) and (25) was calculated using the daily time series of each variable and a 31-day moving average was then applied to construct the MLS (section 3b) and MLT (section 3c) budgets. The estimation of an error for each term in Eqs. (24) and (25) is given in appendix A, and the residual terms to the MLS and MLT budgets are discussed in appendix B.

3. Results

As described in section 1, the three SPURS-2 moorings were located within the EPFP (SSS < 34.0; Alory et al. 2012; Guimbard et al. 2017) and north of the SSS front that was the focus of the KS2020 study (Fig. 1). The southwestward trade wind prevails in boreal winter and spring while the northeastward wind prevails in boreal summer and autumn associated with northward migration of the ITCZ (Guimbard et al. 2017; KS2020). The seasonal climatology of KS2020 showed strong surface freshening by precipitation at the location of the SPURS-2 moorings occurs during boreal summer and autumn, which reflects the seasonality of the ITCZ. The EPFP shrinks eastward in winter (Fig. 1a) and extends westward in summer (Fig. 1b). The SPURS-2 moorings were located in the gap between the western and eastern Pacific warm pools (KS2020), and within the meridional maximum of SST (>28°C) in summer (Fig. 1b) that migrates southward in winter (Fig. 1a). The SPURS-2 moorings were also located in a transition zone between the westward North Equatorial Current (NEC) to the north and the eastward North Equatorial Countercurrent (NECC) to the south (e.g., Farrar and Plueddemann 2019; Katsura et al. 2021). Along the 125°W longitude of the SPURS-2 moorings, the NEC is strong in winter and weak in summer and migrates northward in autumn and southward in spring (Liu and Zhou 2020). The NECC is strong (weak) and migrates northward (southward) in summer–autumn (winter–spring) in the eastern tropical Pacific (Hsin and Qiu 2012).

Figure 2 shows the different scenarios that might result in BL and TI formation. In the EPFP and at the SSS front, the contribution of the horizontal SST gradient to the horizontal density gradient is smaller than that of the horizontal SSS gradient (KS2020; Katsura et al. 2021), which is favorable for BL formation through horizontal advection (Fig. 2b). In addition, SSS decreases and SST increases north of the SSS front (KS2020; Katsura et al. 2021), which is favorable for TI formation through horizontal advection (Fig. 2d). During the SPURS-2 mooring deployments, both zonal and meridional SSS gradients were dominant contributors to the density gradient almost throughout the entire observation period at the mooring sites (not shown), indicating that the horizontal advection of freshwater can result in BL and TI formation (Fig. 2b).

In the following subsections, we will explore the features of BLs and TIs in the EPFP and their formation and subsequent effect on the MLS and MLT budget.

a. BLs and TIs at SPURS-2 moorings

BLs and TIs at the SPURS-2 moorings showed seasonality in their formation with most occurring in boreal summer and autumn, consistent with the climatological study in the same region (KS2020). At the WHOI mooring (10°N, 125°W), the ILD was ~50 dbar in September–October 2016 (Figs. 3a,b). The isothermal layer shoaled in boreal autumn and was only ~20 dbar in December 2016. During boreal winter and spring in January–May 2017, the isothermal layer deepened and reached 75 dbar. The isothermal layer shoaled rapidly to ~20 dbar over June 2017, but then deepened to around 50 dbar during boreal summer and autumn (July–October) in 2017. Likewise, MLD at the WHOI mooring was around 30 dbar during boreal autumn in September–December 2016 and deepened during boreal winter and spring in January–May 2017 reaching 75 dbar (Figs. 3a,b). The mixed layer shoaled in June 2017 and then stayed around 40 dbar. During the boreal summer–autumn in September–December 2016, salinity within the mixed layer was lower than 33.5 (Fig. 3a). This freshening of the surface layer caused a shallower MLD compared to the ILD, resulting in BLs in September–December 2016 (Figs. 3a–c). During this period, TIs were found within the BLs with a peak amplitude of $\Delta\theta > 0.5$°C in October 2016 (Figs. 3b,c). Surface layer salinity was again <34.0 in June–October 2017, leading to BLTs of nearly 40 dbar (Fig. 3c). TIs were also observed during this period, showing peaks occurrences in the middle of July, the end of August, and the middle of October with $\Delta\theta > 0.3$°C.

To the north, BLs at the PICOSP01 mooring (11°N, 125°W) showed a seasonality that is consistent with that at the WHOI mooring, although the TIs were not as frequently observed at the PICOSP01 mooring (Fig. 4). The ILD at the PICOSP01 mooring was around 25 dbar during summer and autumn in August–December 2016, then deepened to ~80 dbar during winter and spring in January–May 2017 and shoaled in June 2017 to 20 dbar (Figs. 4a,b). As at the WHOI mooring, the variation of MLD at the PICOSP01 mooring followed that of the ILD. The MLD ranged from 10 to 30 dbar during summer and autumn in August–December 2016, deepened during winter and spring in January–May 2017 to 80 dbar, and then shoaled to 10 dbar in June 2017. Surface layer salinity was lower than 34.0 in August–December 2016 (Fig. 4a), causing a shallower MLD and hence BL formation (Fig. 4c). BLT exceeded 10 dbar in September 2016 and decayed in January 2017. When MLD and ILD shoaled in June 2017, BLs were also observed with a maximum BLT ~20 dbar occurring at the end of June 2017. TIs at the PICOSP01 mooring were detected less frequently, and the amplitude of the

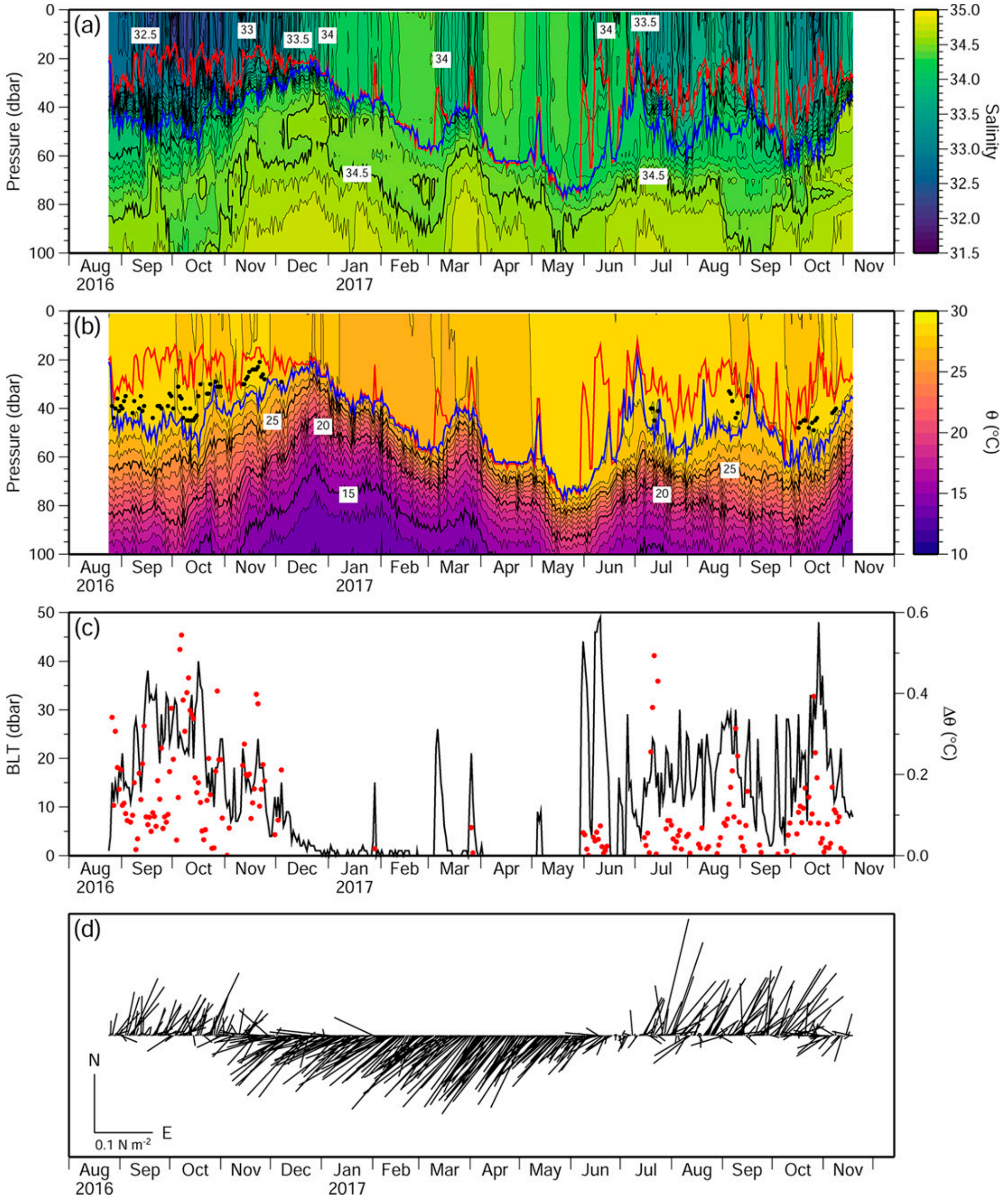

FIG. 3. Daily time series of the vertical profile of (a) salinity, (b) θ (°C), (c) BLT (dbar; black curve) and $\Delta\theta$ (°C; red dots), and (d) wind stress $\boldsymbol{\tau}_0$ (N m^{-2}) at the WHOI mooring. Red and blue lines in (a) and (b) indicate the MLD and ILD, respectively. Black dots in (b) denote the depth of the vertical temperature maximum where $\Delta\theta > 0.1$°C.

TIs was smaller than at the WHOI mooring both in summer–autumn 2016 and in summer 2017.

To the south, BLs and TIs at the PICOSP02 mooring showed the same seasonality as the other two moorings, and their amplitude was comparable to the WHOI mooring (Fig. 5). ILD deepened from 20 dbar in August 2016 to 70 dbar in October 2016, shoaled during autumn in October–December 2016 to 40 dbar, deepened again during winter and spring in January–May 2017 to 70 dbar, then slightly shoaled to ~60 dbar during summer and autumn in June–October 2017 (Figs. 5a,b). MLD varied from 10 to 45 dbar and was shallower than the ILD during summer and autumn in August–December 2016 due to the presence of low-salinity water (<34.0), leading to BL formation (Fig. 5c). MLD deepened during winter and spring in January–May 2017 together with the ILD, and BLs decayed. MLD shoaled to 10 dbar in June 2017 in association with low-salinity water in the mixed layer (<34.0). MLD ranged from 10 to 70 dbar during summer

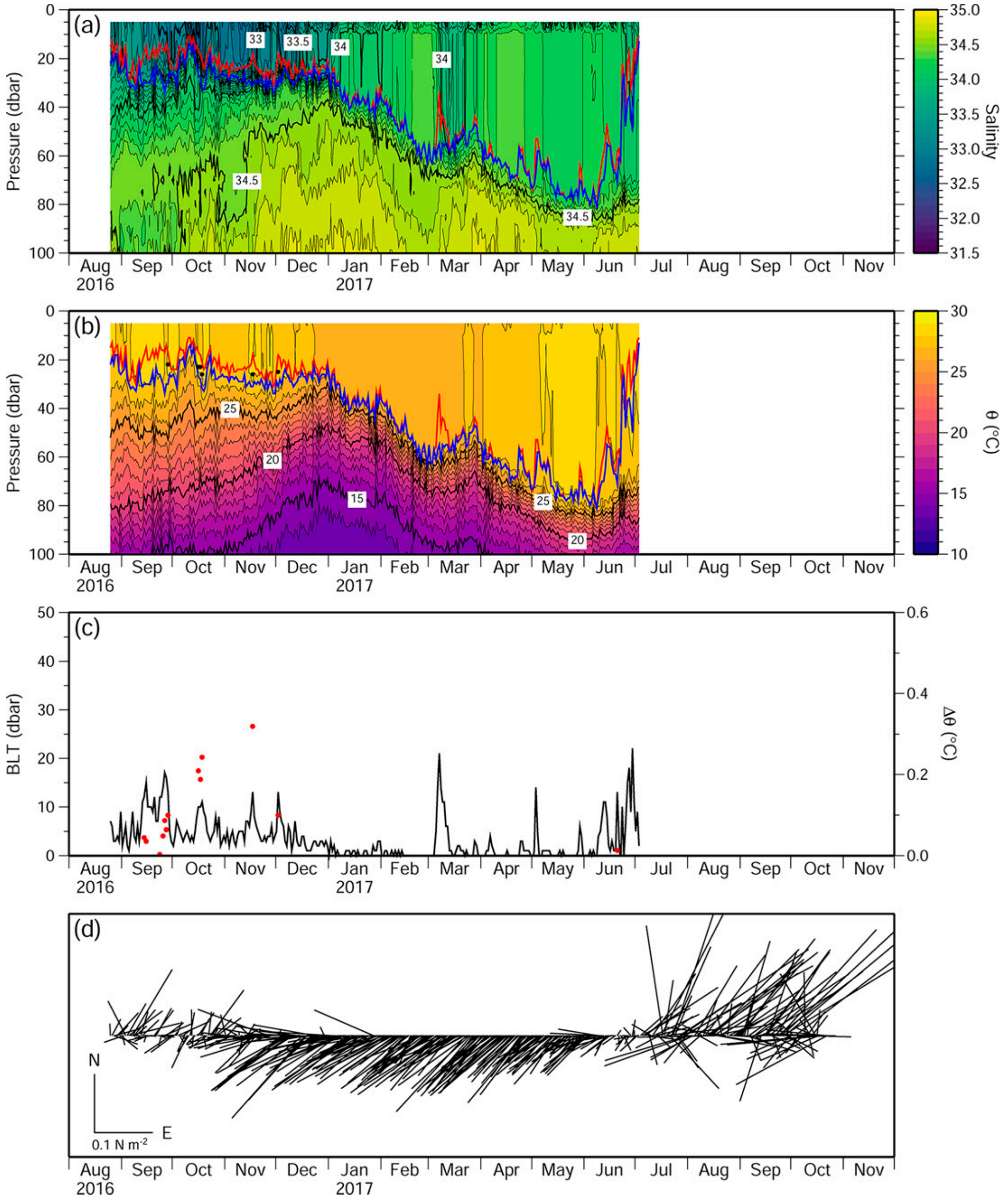

FIG. 4. As in Fig. 3, but for the PICOSP01 mooring. Wind stress $\boldsymbol{\tau}_0$ in (d) is from CCMP.

and autumn in June–October 2017 and BLs with TIs were detected over this period (Figs. 5b,c). TIs formed within BLs during summer and autumn in August–December 2016, occasionally reaching $\Delta\theta > 0.3$°C. TIs disappeared in January 2017 with the decay of the BLs but reemerged at the end of May 2017 and persisted during summer and autumn in June–October 2017.

The seasonality of BLs and TIs at the SPURS-2 moorings was largely consistent with the seasonal climatology (KS2020). However, the BL presence persisted during the boreal summer and autumn at all three SPURS-2 moorings (Figs. 3c, 4c, and 5c). in contrast to the patchiness of the BL formation observed during the two SPURS-2 cruises that also occurred in these seasons (Katsura et al. 2021). The periods in which BLs and TIs were observed at the SPURS-2 moorings corresponded to periods of northeastward wind during summer and autumn (August–November) in 2016 (Figs. 3d, 4d, and 5d). Southwestward winds existed during winter and spring (December–May 2017), returning to northeastward in summer and autumn (June–October 2017). KS2020 showed that the northeastward wind causes southeastward Ekman advection across the SSS front located south of the EPFP, resulting in both surface freshening and cooling and hence BL and TI formation

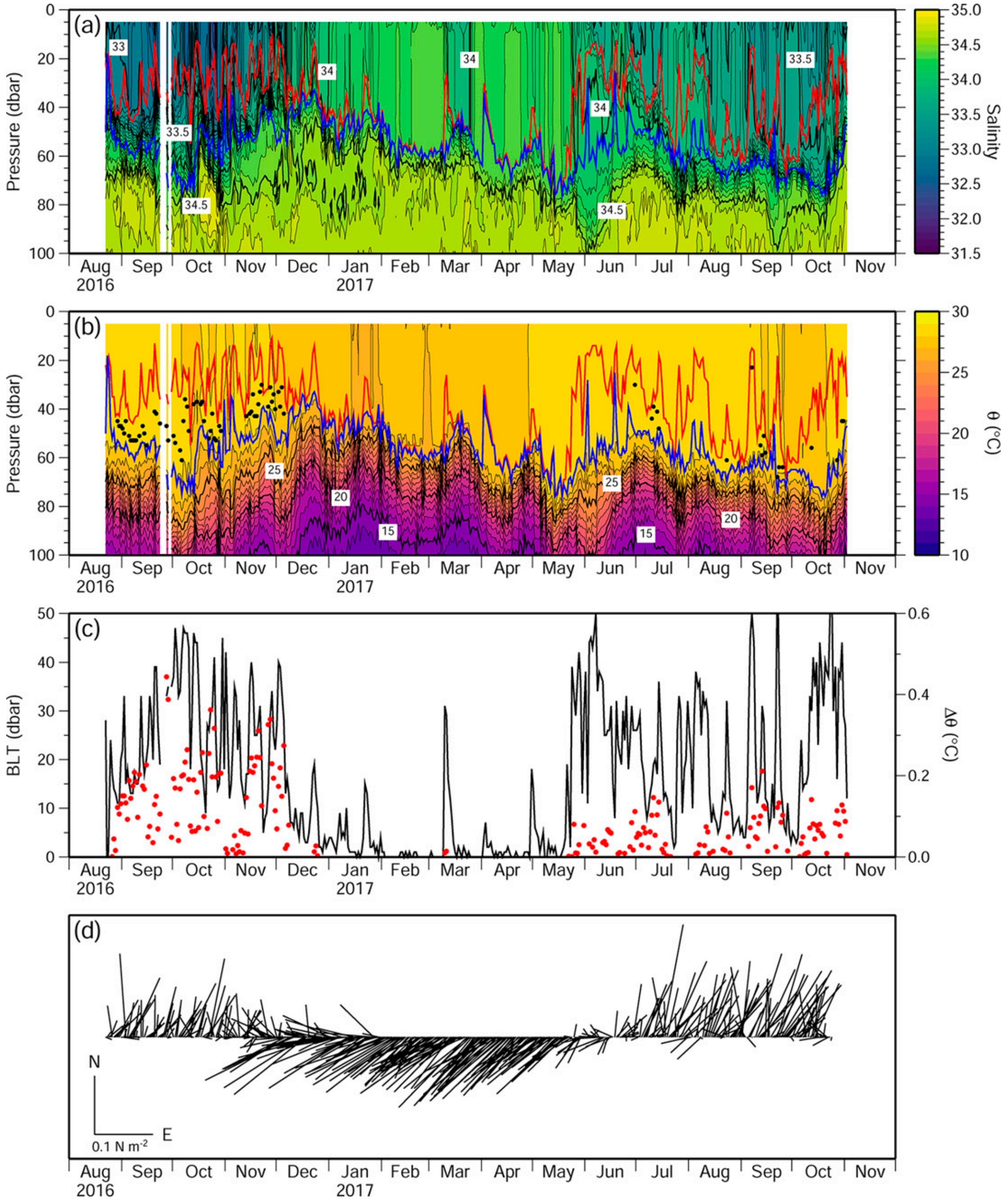

FIG. 5. As in Fig. 3, but for the PICOSP02 mooring. Wind stress $\boldsymbol{\tau}_0$ in (d) is from CCMP.

through the tilting of the SSS front. BLs with BLT > 20 dbar were also observed in the middle of March 2017 at the three moorings (Figs. 3c, 4c, and 5c). This BL formation in March 2017 was associated with a distinct and unusual surface freshening ($S < 34.0$) event at the three moorings (Figs. 3a, 4a, and 5a) that was not evident in the climatology (KS2020).

b. MLS budget and BL formation

To determine the formation mechanisms of BLs observed at the three SPURS-2 moorings, an MLS budget was constructed using Eq. (24). Here, we focus on BL formation through surface freshening. Appendix B will discuss the contribution of missing processes to the residual terms. In general, the tendency of the MLS [$\partial S_m/\partial t$; the left-hand side of Eq. (24)] showed good agreement with the sum of the forcing terms [the right-hand side of Eq. (24)] at the three SPURS-2 moorings although a mismatch was found during some periods (Figs. 6a, 7a, and 8a). At all three SPURS-2 moorings, the MLS tendency largely corresponded to the variation of BLT. For example, the MLS tendency was negative from September to the middle of October 2016 (Figs. 6a, 7a, and 8a) when BLT increased (Figs. 3c, 4c, and 5c), while after

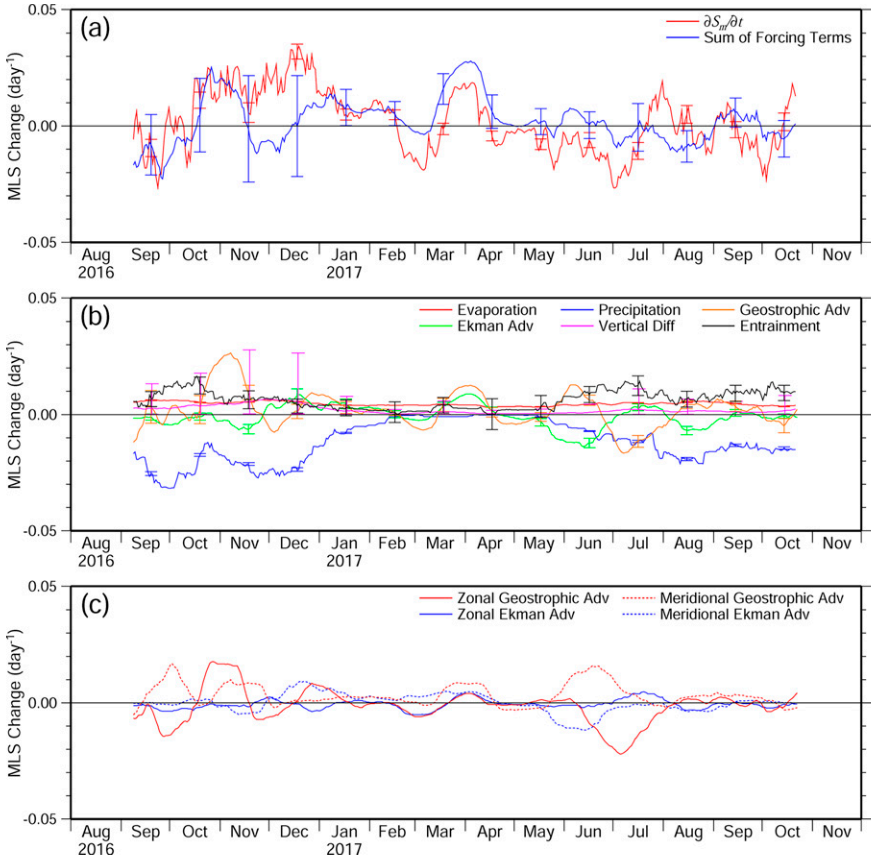

FIG. 6. Time series at the WHOI mooring of the 31-day moving-averaged (a) $\partial S_m/\partial t$ (day^{-1}; red), and the sum of forcing terms (blue), and (b) each forcing term: evaporation (red), precipitation (blue), Ekman advection (green), geostrophic advection (orange), vertical diffusion (magenta), and entrainment (black). (c) Time series of zonal (solid line) and meridional (dashed line) components of the 31-day moving-averaged geostrophic (red) and Ekman (blue) advection terms.

October 2016, the MLS tendency became positive, and BLT decreased. Around May and June 2017, BLs started developing again and the MLS tendency became negative again. These results indicate that the BL formation and the variation of BLT at the SPURS-2 moorings were dominated by surface freshening.

Precipitation was a prime contributor to the surface freshening at the SPURS-2 moorings and showed a seasonality corresponding to the presence of BLs. Surface freshening was dominated by precipitation from September to December 2016 and again from June to October 2017 (Figs. 6b, 7b, and 8b) when BLs were observed, and precipitation was small during January–May 2017 when BLs decayed, reflecting the seasonality of the ITCZ (Figs. 3c, 4c, and 5c). At the PICOSP01 mooring, precipitation freshening during the summer and autumn was small compared to the other two moorings, corresponding to thin BLs. These results indicate that precipitation contributed to the BL formation and maintenance through surface freshening during summer and autumn at the SPURS-2 moorings.

Horizontal advection was a secondary contributor to the surface freshening and the BL formation at the SPURS-2 moorings. Strong freshening by geostrophic advection was observed around March 2017 at all SPURS-2 moorings (Figs. 6b, 7b, and 8b) when BLT was >20 dbar (Figs. 3c, 4c, and 5c). The geostrophic advection was dominated by the zonal component at the WHOI and PICOSP01 mooring (Figs. 6c and 7c) that was driven by the westward NEC (not shown), while the meridional component was a dominant contributor to surface freshening at the PICOSP02 mooring (Fig. 8c) that was driven by southward flow (not shown). At the WHOI mooring, freshening by Ekman advection was large in June 2017 when BLs started developing and BLT > 40 dbar (Figs. 3c and 6b). This Ekman freshening in June 2017 was dominated by the meridional component resulting from northward Ekman flow driven by the southwestward trade wind (Figs. 3d and 6c). There is a strong intraseasonal oscillation in geostrophic advection, consistent with resonant forcing associated with the westward passage of cyclonic winds (Mickett et al. 2010), and previous observations of intraseasonal eddy/wave variability at this site (Farrar and Weller 2006; Hasson et al. 2019). Zonal geostrophic advection also worked to freshen the mixed layer from the end of June to the middle of August 2017

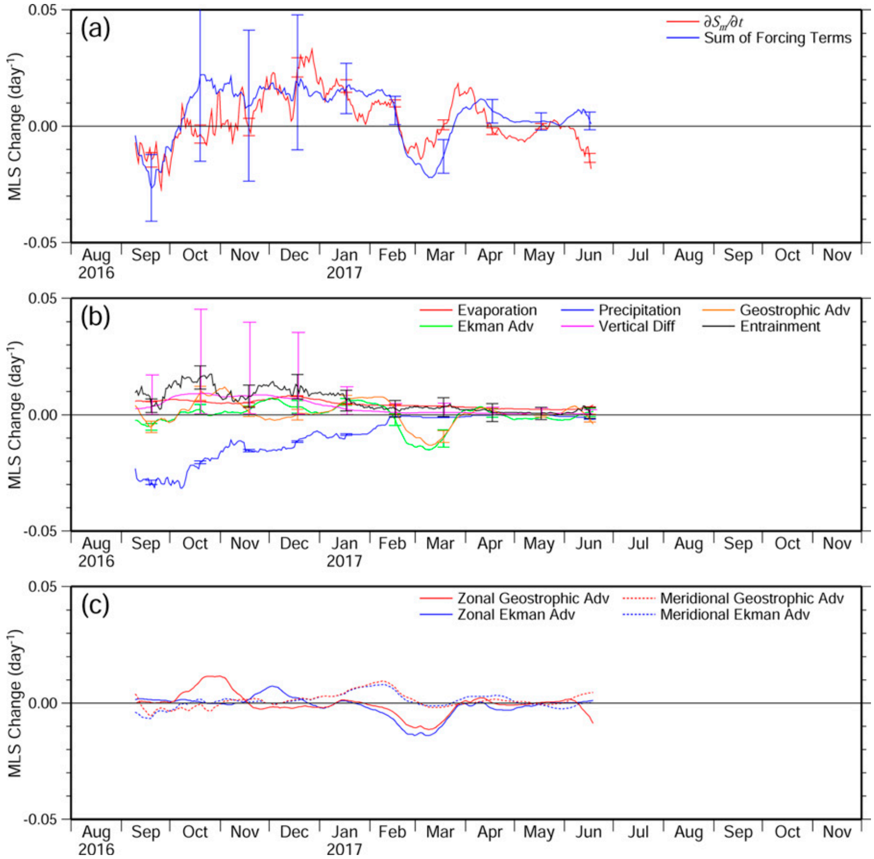

FIG. 7. As in Fig. 6, but for the PICOSP01 mooring.

(Figs. 6b,c). This zonal geostrophic advection was driven by westward flow, which could be the NEC or a northern flank of a cyclonic eddy centered at ~8.5°N, 123°W, as identified in the OSCAR current field (not shown). At the PICOSP02 mooring, freshening by Ekman and geostrophic advection, dominated by meridional and zonal flow, respectively, was large in May–June 2017 corresponding to the beginning of BL formation (Figs. 5c, 8b, and 8c). At both these moorings, freshening by horizontal advection was exceeded by precipitation during the summer and autumn (Figs. 6b and 8b). These results indicate that horizontal advection was the secondary contributor to the surface freshening and hence the BL formation at the SPURS-2 mooring. In particular, it appears that horizontal advection contributed to the initial formation of BLs in summer 2017, and then the formed BLs were maintained through surface freshening by precipitation.

Both evaporation and vertical diffusion worked to increase MLS but played only a minor role in the MLS budget at the SPURS-2 moorings (Figs. 6b, 7b, and 8b). Entrainment also contributed to salinification of the surface mixed layer. The contribution of entrainment to the MLS budget was large in summer and autumn when BLs were observed and small in winter and spring. This correspondence reflects the intensification of salinity stratification at the mixed layer base.

In summary, the MLS budget analysis indicated that precipitation is the prime contributor to the BL formation at the SPURS-2 moorings in boreal summer and autumn. Horizontal advection plays a secondary role in BL formation, and its contribution is largest in early summer when the BLs are first developing. These results contrast with the KS2020 climatological study that showed tilting of the SSS front by horizontal advection was the leading mechanism of BL formation while precipitation was a secondary contributor to BL formation. This discrepancy is probably due to the location of the SPURS-2 moorings, well north of the SSS front (~7°N; Fig. 1). The SPURS-2 moorings were located within the EPFP where a dominant contribution of precipitation to the BL formation was observed during two SPURS-2 cruises in 2016 boreal summer and in 2017 boreal autumn (Katsura et al. 2021). Indeed, at the PICOSP02 mooring, which at 9°N is the southernmost among the SPURS-2 moorings, Ekman advection contributed to the BL formation in autumn 2016 and in early summer 2017 (Fig. 8b). The interannual variability of wind might also result in the weaker freshening by Ekman advection at the SPURS-2 moorings.

c. *MLT budget and TI formation*

To evaluate the formation mechanism of TIs associated with BLs at the SPURS-2 moorings, an MLT budget was constructed using Eq. (25). Appendix B will discuss the contribution of missing processes in the residual terms. Here, we focus

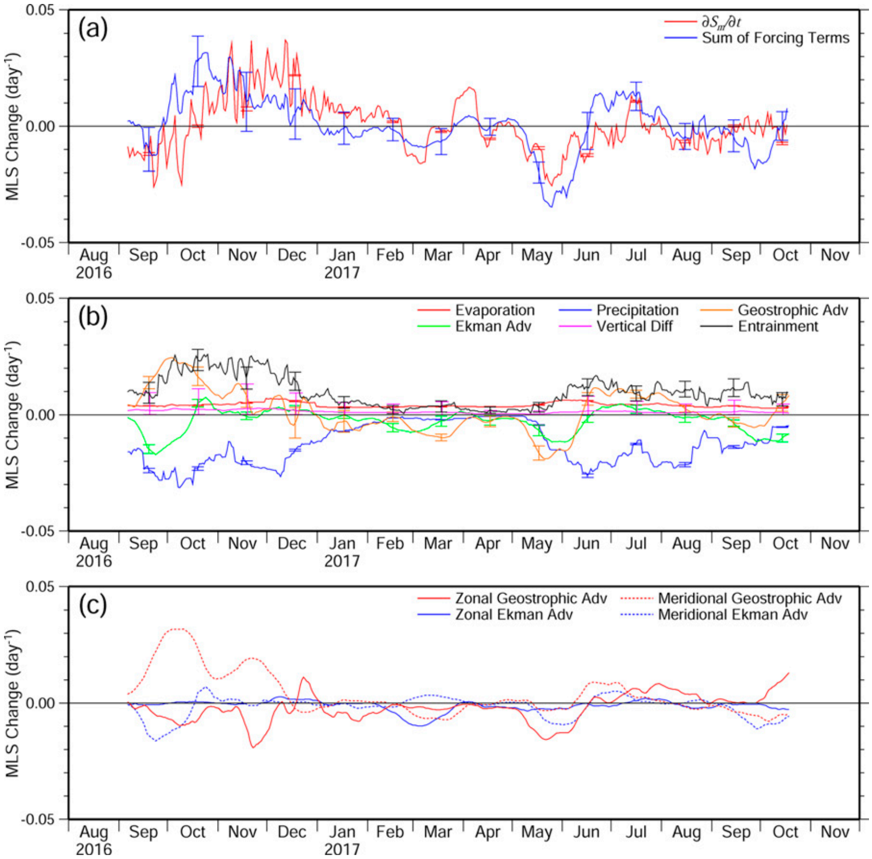

FIG. 8. As in Fig. 6, but for the PICOSP02 mooring.

on the TI formation through surface cooling. As for the MLS budget, in general the MLT tendency [$\partial T_m/\partial t$; the left-hand side of Eq. (25)] and the sum of the forcing terms [the right-hand side of Eq. (25)] showed a relatively good agreement at the three SPURS-2 moorings, and the MLT budget generally reproduced the MLT variability (Figs. 9a, 10a, and 11a). The largest discrepancy between the forcing terms and the tendency terms at all three moorings occurred primarily at the beginning of the observational record in September–October 2016.

Penetration of shortwave radiation was a major contributor to surface cooling at the SPURS-2 moorings during the period when BLs and TIs were observed, and its variation corresponded to the seasonality of TIs. Shortwave penetration largely contributed to the mixed layer cooling during September–December 2016, became smaller from January–May 2017 and then increased again after June 2017 (Figs. 9b, 10b, and 11b). During these periods, the MLT tendency ($\partial T_m/\partial t$) was nearly zero and much smaller than the shortwave penetration term, indicating that in the mixed layer, warming by shortwave penetration was balanced by other forcing terms, but in the underlying layer the penetration of shortwave radiation causes warming relative to the mixed layer. This seasonality of cooling by shortwave penetration was influenced by the seasonality of the MLD and corresponded well to the presence of TIs at the SPURS-2 moorings (Figs. 3c, 4c, 5c), indicating that shortwave radiation penetrates beyond the mixed layer base and the heat is thus available for TI formation.

Geostrophic advection also worked to cool the mixed layer occasionally at the SPURS-2 moorings, while Ekman advection had little impact or mostly acted to warm the MLT. At the WHOI mooring, zonal geostrophic advection driven by the eastward NECC (not shown) contributed to surface cooling from mid-October to mid-December 2016 but contributed to mixed layer warming during the rest of the year (Figs. 9b,c). Both Ekman and geostrophic advection were small or acted to warm the MLT at the PICOSP01 mooring (Fig. 10b), indicating that horizontal advection did not contribute to the TI formation. At the PICOSP02 mooring, geostrophic advection contributed to the surface cooling and the TI formation in September–October 2016 and again in June 2017, although the cooling effect from advection was smaller than that of shortwave penetration (Fig. 11b). In fact, at all three moorings, the cooling by geostrophic advection was weak compared to the shortwave penetration impact, indicating that geostrophic advection plays a secondary role in TI formation and Ekman advection plays only a minor role.

While the net heat flux term was the largest contributor to the MLT budget at all three SPURS-2 moorings, it mostly worked to warm the mixed layer and so did not contribute to the TI formation (Figs. 9b, 10b, 11b). At the PICOSP01 and PICOSP02 moorings, net heat flux warmed the mixed layer

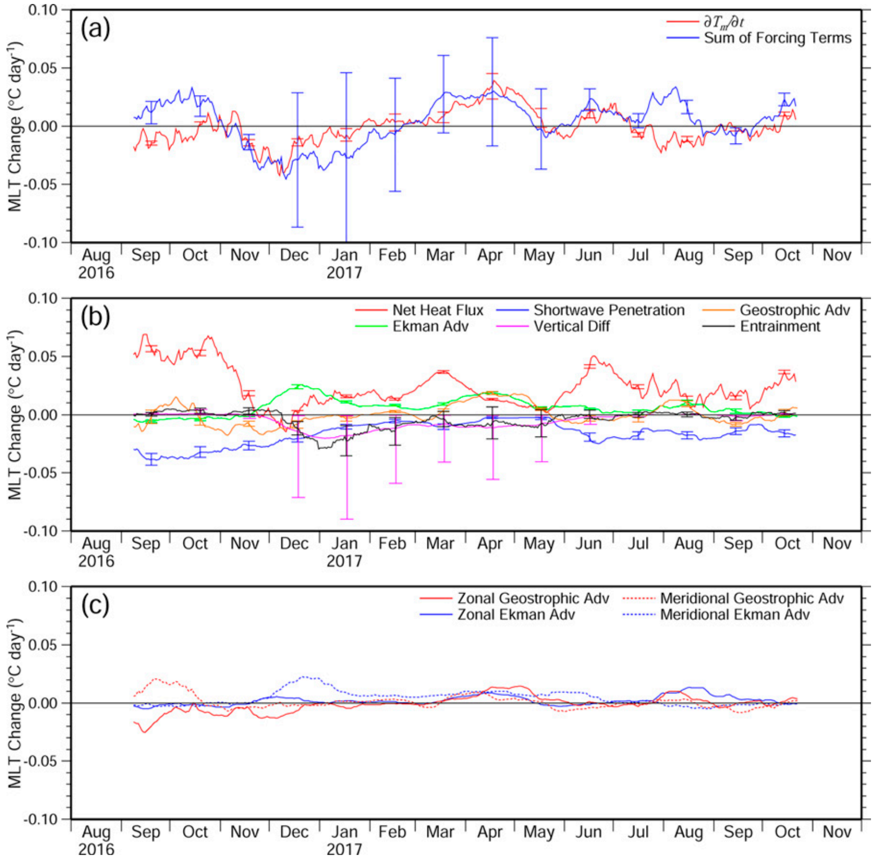

FIG. 9. Time series at the WHOI mooring of the 31-day moving-averaged (a) $\partial T_m/\partial t$ (°C day^{-1}; red) and the sum of forcing terms (blue), and (b) each forcing term: net heat flux (red), shortwave penetration (blue), Ekman advection (green), geostrophic advection (orange), vertical diffusion (magenta), and entrainment (black). (c) Time series of zonal (solid) and meridional (dashed) components of the 31-day moving-averaged geostrophic (red) and Ekman (blue) advection terms.

throughout the observation period except around December 2016 (Figs. 10b and 11b). Although vertical diffusion and entrainment terms in the MLT budget at the SPURS-2 moorings showed a seasonality corresponding to that of the presence of BLs and TIs, the sign of these terms over the record suggested they played little role in formation of either BLs or TIs. At the three SPURS-2 moorings, both vertical diffusion and entrainment contributed to the mixed layer cooling during December 2016–May 2017 (Figs. 9b, 10b, and 11b) when BLs and TIs were not observed (Figs. 3c, 4c, and 5c). On the other hand, the contribution of vertical diffusion and entrainment to the MLT budget was nearly zero or slightly positive (warming) during September–November 2016 and June–October 2017 when BLs and TIs were observed. This implies that the cooling effect from entrainment and vertical diffusion was reduced by the persistent existence of BLs and TIs during these periods (Figs. 3c, 4c, and 5c). Although vertical diffusion and entrainment acted to cool the mixed layer during December 2016–May 2017, these processes cannot contribute to TI formation because vertical diffusion and entrainment processes work to homogenize the temperature difference between the mixed layer and the underlying layer.

In summary, penetration of shortwave radiation was a prime contributor to the TI formation through the cooling of the surface mixed layer relative to the underlying layer (i.e., subsurface warming). Geostrophic advection also contributed to the surface cooling and occasionally to TI formation. Cooling by vertical diffusion and entrainment was reduced during the period when BLs and TIs were observed. In September–November 2016 and in June–October 2017 when TIs and BLs were found, the MLT tendency was almost zero, and the presence of TIs was not associated with the mixed layer cooling (Figs. 9a, 10a, and 11a). This can be explained by the dominant contribution of shortwave penetration which leads to TI formation through subsurface warming rather than surface cooling. At the northern-most PICOSP01 mooring, BLs with TI were not observed as frequently as at the other two moorings although the cooling by shortwave penetration was comparable to that at the PICOSP02 mooring and larger than at the WHOI mooring. This is probably because the MLS during

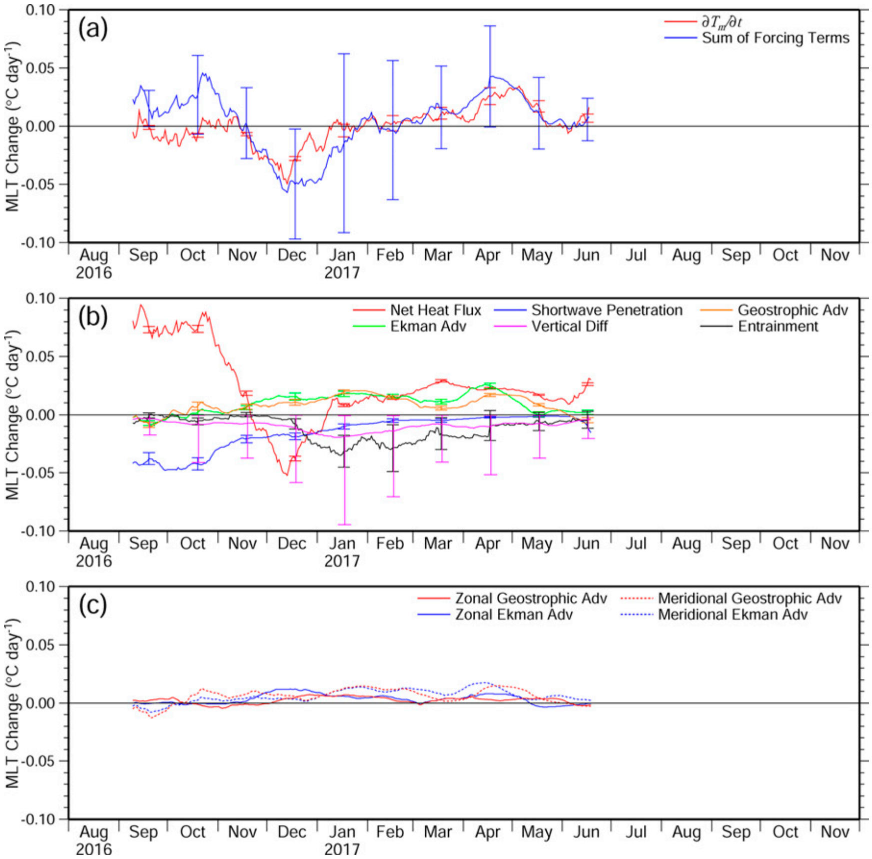

FIG. 10. As in Fig. 9, but for the PICOSP01 mooring.

the periods when BLs were present was higher at the PICOSP01 mooring ($S_m > 33.0$) than at the WHOI and PICOSP02 moorings ($S_m < 33.0$) in September–October 2016, and hence the salinity stratification was not strong enough to compensate the density instability associated with TIs.

d. Impact of BLs and TIs on entrainment and surface flux terms

The MLT budget in section 3c revealed that the cooling effect by entrainment was small during the period when BLs and TIs were present. To further evaluate the impact of BLs and TIs on the entrainment cooling effect, a scatter diagram was constructed of the entrainment term [Eq. (21)] versus the deepening rate D [Eq. (22)] for the three SPURS-2 moorings based on the daily time series (Fig. 12). For the entrainment cases ($D > 0$), the entrainment cooling was significantly reduced by the presence of a BL, and the entrainment effect turned to warming (positive) when TIs existed. At the WHOI mooring, entrainment worked to cool the mixed layer when BLT $<$ 10 dbar, and the cooling effect by entrainment increased with the deepening rate (Fig. 12a). When BLs with BLT $>$ 10 dbar existed, the entrainment cooling was greatly reduced, and the regression coefficient (-0.02) was an order of magnitude below that for cases without BLs (-0.28). When BLs were associated with TIs, the regression coefficient was positive (0.07), and entrainment worked to warm the mixed layer. Similar tendencies of the entrainment term and the deepening rate for BL and TI presence were also found for the PICOSP01 and PICOSP02 moorings (Figs. 12b,c). The effect of BLs to reduce the entrainment cooling was larger at the PICOSP02 mooring (Fig. 12c) where BLs were thick compared to the WHOI mooring (Fig. 12a), and smaller at the PICOSP01 mooring where BLs were thin (Fig. 12b). These results indicated that entrainment cooling is significantly reduced by the presence of BLs, and the associated TIs worked to warm the mixed layer through that entrainment. This suggests that the BLT is an important factor impacting entrainment cooling (Foltz and McPhaden 2009; Yan et al. 2017).

Detrainment ($D < 0$) worked to warm the mixed layer separating the cooler water from the mixed layer (Fig. 12). The warming effect of the detrainment was reduced when BLs were present (Fig. 12). At the WHOI mooring, detrainment contributed to the mixed layer warming, and this detrainment warming was reduced when BLT $>$ 10 dbar compared to when BLT $<$ 10 dbar (Fig. 12a). Similar detrainment warming effects were found at the PICOSP01 and PICOSP02 moorings, and the warming effect of detrainment was small when BLs existed (Figs. 12b,c). These results indicate that the existence of the BL affects not only the entrainment cooling but also the detrainment warming. At the WHOI and PICOSP02

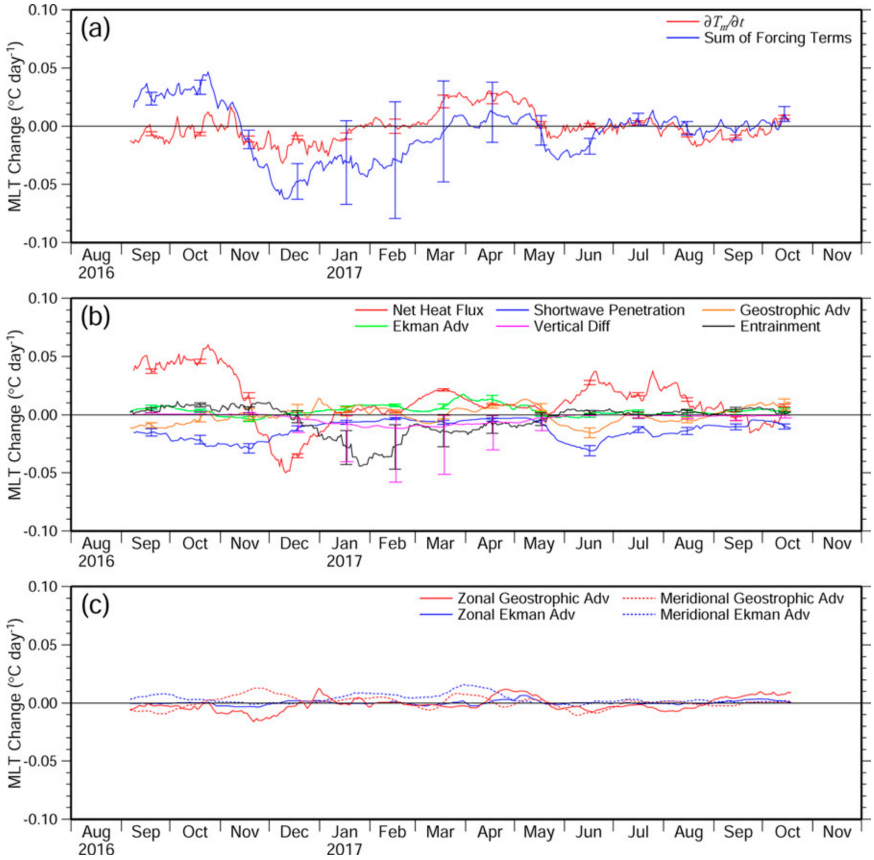

FIG. 11. As in Fig. 9, but for the PICOSP02 mooring.

moorings, reduced detrainment warming did not show any significant difference between cases with and without TIs (Figs. 12a,c). This is because the detrainment process associated with mixed layer shoaling is independent of the vertical temperature structure below the mixed layer.

The existence of BLs also affected the sensitivity of the mixed layer to the surface heat flux (Figs. 13a,c). The contribution of net heat flux to warming of the mixed layer was significantly larger when BLT > 10 dbar than when BLT < 10 dbar (Fig. 13a). The surface cooling relative to the subsurface by

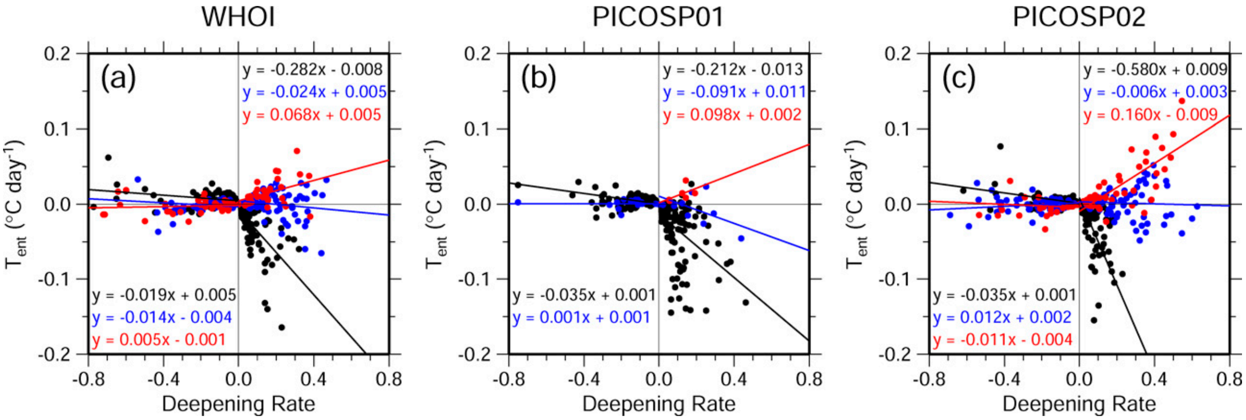

FIG. 12. Scatter diagram of T_{ent} (°C day^{-1}) calculated as part of the MLT budget and the deepening rate based on the daily time series at the (a) WHOI, (b) PICOSP01, and (c) PICOSP02 moorings. Black dots indicate the cases for BLT < 10 dbar. Blue dots indicate the cases for BLT > 10 dbar and $\Delta\theta < 0.1$°C. Red dots indicate the cases for BLT > 10 dbar and $\Delta\theta > 0.1$°C. Black, blue, and red lines indicate the regression lines for each case calculated for positive and negative deepening rate.

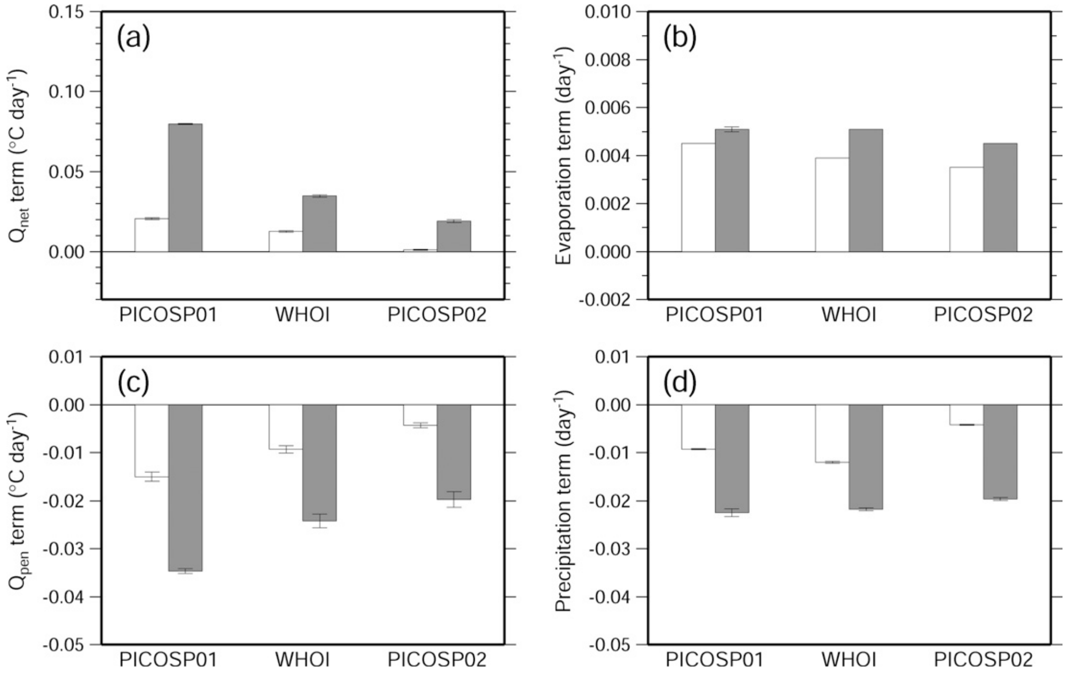

FIG. 13. Mean values of temperature change (°C day^{-1}) due to (a) net surface heat flux and (c) penetration of shortwave radiation and salinity change (day^{-1}) due to (b) evaporation and (d) precipitation terms at each mooring averaged for BLT < 10 dbar (white bars) and for BLT > 10 dbar (gray bars) based on the daily time series.

the shortwave penetration was also large when thick BLs were present compared to the cases without thick BLs (Fig. 13c). This difference in the sensitivity of the mixed layer to the surface heat flux was due to the shallower mixed layer associated with the presence of a BL. In particular, the strong surface cooling by the penetration of the shortwave radiation associated with BLs implied that the existence of BLs assisted the TI formation through subsurface warming brought about by shortwave penetration.

The surface freshwater flux terms (evaporation and precipitation) were also large depending on the presence of BLs (Figs. 13b,d). The evaporation term at the SPURS-2 moorings was slightly larger when BLs were present than when they were absent (Fig. 13b), indicating that the mixed layer became more sensitive to evaporation due to the BL presence. Larger freshening of the mixed layer by precipitation was also found when BLs were present (Fig. 13d). However, this approach cannot distinguish the cause and effect between precipitation and BLs. That is, we cannot determine if strong freshening by precipitation contributed to the presence of thick BLs, and/or vice versa.

4. Discussion and summary

BLs and associated TIs were investigated using the 1-yr-long time series from the three SPURS-2 moorings that were deployed in the EPFP. BLs at the SPURS-2 moorings were thickest in boreal summer and autumn and decayed in boreal winter and spring, which is consistent with the seasonal climatology (KS2020). However, BLs were a persistent feature in the mooring time series during these seasons in contrast to the patchy distribution of BLs observed during the two SPURS-2 cruises in late summer 2016 and autumn 2017 (Katsura et al. 2021). BLs were associated with TIs in boreal summer and autumn at the WHOI and PICOSP02 moorings while TIs were less frequently observed at the northernmost PICOSP01 mooring. Salinity within the surface mixed layer was low during boreal summer and autumn when BLs were observed compared to the periods without BLs.

To investigate the mechanisms of BL formation and maintenance at the SPURS-2 moorings, an MLS budget analysis was constructed. The MLS tendency largely corresponded to the variation of BLT at the SPURS-2 moorings, indicating that formation and maintenance of BLs were dominated by surface freshening. Precipitation was a prime contributor to the surface freshening, and seasonally corresponded to the seasonality of BLs. Horizontal advection was a secondary contributor to surface freshening, and its freshening effect was occasionally large especially in summer 2017 when BLs started developing. These results indicated that BLs were likely initially formed by horizontal advection and then maintained through surface freshening by precipitation. The contribution of entrainment to the MLS budget was large in summer and autumn, when BLs were observed. Further east at 95°W, Mickett et al. (2010) found increased turbulent energy associated with near-inertial resonant forcing by atmospheric tropical cyclones in boreal summer, this process may also influence entrainment at our mooring sites.

The unusual presence of the BLs in March 2017 is related to an episodic event of strong surface freshening through geostrophic advection. In the eastern tropical North Pacific, mesoscale eddies can cause large SSS anomalies by horizontal advection at their edges (Delcroix et al. 2019) and by trapping and transporting water within their cores (Hasson et al. 2019). Tropical instability waves are also known to cause strong SSS anomalies in the eastern tropical Pacific (Lee et al. 2012; Yin et al. 2014). The strong surface freshening and associated BL formation in March 2017 at the SPURS-2 moorings may be caused by these small-scale phenomena. Considering that the BLs have a significant impact on the MLT budget as shown in this study, these small-scale ocean dynamics may affect the air–sea interaction through the BL formation. Further investigation of the relationship of BLs and ocean dynamics on small spatiotemporal scales is the subject of future work.

This study investigated BL formation based on the MLS and MLT budgets (Fig. 2); however, there are missing processes from our budgets that can cause BLs. To determine BL formation through the tilting process, measurements of the vertical shear of horizontal velocity within the isothermal layer is needed (Fig. 2b). While a horizontal velocity profile was measured at the WHOI mooring, at the PICOSP moorings, recall that the horizontal currents were not directly measured and so the Ekman velocity $\mathbf{u}_{\mathrm{Ek}}$ was computed as the OSCAR current minus geostrophic velocity $\mathbf{u}_g$ estimated from the SSH gradient. At the WHOI mooring, we estimated the tilting terms (KS2020) and found that the salinity tilting term was negative in February–March and June 2017 (not shown) when geostrophic and Ekman advection also contributed to surface freshening and BL formation (Fig. 6b). This indicates that the surface freshening caused by the horizontal advection during these periods was associated with the tilting of isohalines resulting in BL formation, although the amplitude of the salinity tilting contribution was smaller than that of geostrophic and Ekman advection (not shown). The temperature tilting term was near zero or positive almost throughout the entire period of the WHOI mooring measurements, indicating that the tilting process did not contribute to the net surface cooling and hence TI formation (not shown). This is consistent with the horizontal advection terms within the MLT, indicating that horizontal advection did not contribute to TI formation (Fig. 9b). BLs can also be advected into a region if the horizontal velocity flows from thick BL regions to thin BL regions (Cronin and McPhaden 2002). This horizontal advection of BLs is not resolved in our observational analysis due to the lack of full three-dimensional fields of subsurface salinity, temperature, and velocity. Another unresolved contributor to the BL formation in this study is the vertical stretching process. When the vertical velocity is not uniform between the MLD and ILD, the BL can grow through vertical stretching (Cronin and McPhaden 2002). To resolve this process, a vertical profile of the vertical velocity is necessary, which was unfortunately unavailable at the SPURS-2 moorings and in fact is difficult to measure in general. High-resolution ocean models might prove useful to pursue the BL and TI formation at small spatiotemporal scales along with unresolved forcing mechanisms not readily obtained through in situ measurements (e.g., Veneziani et al. 2014; Saha et al. 2021).

An MLT budget showed that penetration of shortwave radiation through the mixed layer base was a dominant contributor to the surface cooling at the SPURS-2 moorings with a seasonality that indicated that TIs were mainly formed by subsurface warming brought about through shortwave penetration. Although cooling by shortwave penetration at the PICOSP01 mooring was comparable to that found at the other two moorings, TIs were less frequently observed. This suggests the importance of surface freshening and the associated salinity stratification to the formation and maintenance of the TIs that compensate the density instability at that site. A secondary contribution to surface cooling and TI formation at all three moorings was through geostrophic advection while Ekman advection did not contribute at all to TI formation. Cooling of the mixed layer by vertical diffusion and entrainment was weak during the period when BLs and TIs were persistently present.

At the three SPURS-2 moorings, the cooling effect from entrainment was largely diminished when the BL was present. When TIs were present, the entrainment effect acted to warm the mixed layer. Detrainment warming was also limited by the existence of BLs. This result indicated that BLs and TIs have a significant impact on the contribution of entrainment cooling and detrainment warming to the MLT budget. In addition, when BLs were present, the contribution from surface heat and freshwater fluxes to the MLT and MLS, respectively, became large compared to when the BLs were absent due to the shallower mixed layer associated with BLs. This implies that the presence of BLs affects the heat and freshwater balance within the mixed layer modifying its sensitivity to surface fluxes. In particular, the existence of BLs assisted the TI formation by enhancing the subsurface warming by shortwave penetration.

In the past, the BL impact on the cooling effect of entrainment has mostly been evaluated as a residual of the MLT budget (e.g., Foltz and McPhaden 2009), so to the best of our knowledge, our study provides the first direct evaluation of how the BL and TI explicitly impacts on the entrainment cooling based on observational data. The method applied in our study will be useful to evaluate the BL impact on entrainment cooling in other BL regions, such as the eastern Indian Ocean where the BL presence is suggested to reduce the entrainment cooling during the active phase of the Madden–Julian oscillation (Drushka et al. 2014; Pujiana and McPhaden 2018). We found that the presence of BLs reduces not only the entrainment cooling but also the detrainment warming. In the past, the contribution of detrainment to the MLT budget, and also to the MLS budget, has been assumed to be negligible because it was assumed that detrainment had only a minor effect on the MLT budget compared to entrainment (Cronin et al. 2015). The reduced detrainment warming by the presence of BLs suggests it may be necessary to revisit the contribution of the detrainment process to the MLT budget. The BL impact on detrainment warming in other oceanic regions is needed for a better understanding of the cause of MLT variation and hence the heat exchange between the atmosphere and the ocean.

In contrast to the patchiness and porosity in the distribution of BLs observed during the 2-month-long discrete SPURS-2 cruises (Katsura et al. 2021) that suggests intermittent formation of BLs, in the time series at the SPURS-2 moorings the BLs showed persistence during boreal summer and autumn (Figs. 3c, 4c, and 5c). The persistence of BLs implies that BLs and TIs in the eastern tropical North Pacific play a significant role in local air–sea interactions on different time scales, as also evident through their demonstrated modification of the MLT budget. For example, the surface temperature anomalies in boreal and autumn in the eastern tropical North Pacific, when BLs and TIs are present, play a critical role in the number and the intensity of tropical cyclones (Jin et al. 2014). Our study suggests that BLs and TIs in the eastern tropical Pacific can potentially contribute to the tropical cyclone genesis and intensity through their impact on the MLT budget. In addition, since the BLs in the EPFP significantly modify the sensitivity of the mixed layer to the surface heat and freshwater fluxes, the presence of BLs can also affect the intensity of the easterly trade winds and hence the ITCZ and the wind–evaporation–SST (WES) feedback (Xie and Philander 1994). Evaluation of the impact of BLs and TIs on the atmosphere is an important future task to better understand their role in air–sea interactions and climate variability.

Acknowledgments. SK is supported by JSPS Overseas Research Fellowships. JS and SK are supported by NASA Grant 80NSSC18K1500. JTF and the mooring deployment were funded by NASA Grants NNX15AG20G and 80NSSC18K1494. DZ is supported by NASA Grant 80NSSC18K1499. This publication is partially funded by the Cooperative Institute for Climate, Ocean, and Ecosystem Studies (CICOES) under NOAA Cooperative Agreement NA20OAR4320271, Contribution 2021-1152. This is PMEL Contribution 5268. The authors are thankful to Kelvin Richards, Bo Qiu, Niklas Schneider, and three anonymous reviewers for their valuable comments.

Data availability statement. The L3 70-km version-4.0 product of the NASA Soil Moisture Active Passive was provided by NASA's Physical Oceanography Distributed Active Archive Center (PO.DAAC; https://podaac.jpl.nasa.gov/dataset/SMAP_RSS_L3_SSS_SMI_8DAY-RUNNINGMEAN_V4). The Advanced Very High Resolution Radiometer product of OISST was provided by the National Oceanic and Atmospheric Administration (NOAA) National Centers for Environmental Information (https://www.ncdc.noaa.gov/oisst). IMERG data were obtained from the NASA Goddard Earth Sciences Data and Information Services Center (https://disc.gsfc.nasa.gov/datasets/GPM_3IMERGDF_06/summary?keywords=%22IMERG%20final%22). CCMP gridded surface vector winds version 2.0 was produced by Remote Sensing Systems (http://www.remss.com/measurements/ccmp/). OSCAR data were provided by NASA's PO.DAAC (https://podaac.jpl.nasa.gov/dataset/OSCAR_L4_OC_third-deg). All data from the SPURS-2 moorings are available from the PO.DACC SPURS-2 webpage (https://podaac-tools.jpl.nasa.gov/drive/files/allData/insitu/L2/spurs2/).

APPENDIX A

Error Estimation of the Mixed Layer Temperature and Salinity Budgets

In sections 3b and 3c, the MLS and MLT budget was conducted using Eqs. (24) and (25). Here, we describe how the error of each term in Eqs. (24) and (25) was calculated following Farrar (2007) and Farrar and Plueddemann (2019) based on the theory of error propagation. We also refer to the instantaneous error of the Improved Meteorological (IMET) system by Colbo and Weller (2009), which is the observational system employed at the WHOI mooring.

The error of MLT, ΔT_m, can be expressed as

$$(\Delta T_m)^2 = \left(\frac{\partial T_m}{\partial h_m}\Delta h_m\right)^2 + \left(\frac{\partial T_m}{\partial \theta}\Delta\theta\right)^2. \tag{A1}$$

Using Eq. (6) and

$$\frac{d}{dx}\int_{u(x)}^{0} f(z)dz = -f(u)\frac{du}{dx}, \tag{A2}$$

the first term on the right-hand side of Eq. (A1) can be written as

$$\frac{\partial T_m}{\partial h_m}\Delta h_m = \theta(h_m)\frac{\Delta h_m}{h_m} - T_m\frac{\Delta h_m}{h_m}, \tag{A3}$$

where $\Delta h_m/h_m$ was assumed to be 0.1 (10%; Farrar 2007).

The vertical interval of temperature and salinity profiles at the WHOI mooring is almost uniform (3 or 5 m) in the upper 100-m layer. Thus, for the WHOI mooring, the second term on the right-hand side of Eq. (A1) was estimated using the raw sensor data as

$$\frac{\partial T_m}{\partial \theta}\Delta\theta = \frac{\Delta\theta}{\sqrt{N}}, \tag{A4}$$

where $\Delta\theta$ is the sensor error of temperature and N is the number of sensors within the mixed layer. Equation (A4) is correct only if the vertical spacing of sensors were uniform. The error of MLS, ΔS_m, at the WHOI mooring was also estimated by developing an analogous Eq. (A4) for salinity. For the PICO moorings, the PRAWLER CTD technology enabled significantly higher vertical resolution temperature and salinity profiles. Hence, the second term on the right-hand side of Eq. (A1) can be written as

$$\frac{\partial T_m}{\partial \theta}\Delta\theta = \frac{\sqrt{\sum_{i=1}^{N}(\Delta\theta)^2}}{N}, \tag{A5}$$

for the MLD and analogously for the MLS, where N is the number of vertically interpolated levels of temperature profile within the mixed layer. For both Eqs. (A4) and (A5), for the MLT we used $\Delta\theta = 0.01°\mathrm{C}$ and for the MLS we used $\Delta S = 0.03$. Finally, the velocity profile at the WHOI mooring also had high vertical resolution, and so an analogous equation (A5) was developed for $\Delta\mathbf{u}_m$, where $\Delta\mathbf{u} = 0.03\ \mathrm{m\ s^{-1}}$.

The error of the net heat flux term in Eq. (25) can be written as

$$\left[\Delta\left(\frac{Q_{\text{net}}}{\rho_0 c_p h_m}\right)\right]^2 = \left(\frac{Q_{\text{net}}}{\rho_0 c_p h_m}\,\frac{\Delta h_m}{h_m}\right)^2 + \left(\frac{\Delta Q_{\text{net}}}{\rho_0 c_p h_m}\right)^2, \tag{A6}$$

where ΔQ_{net} is calculated as

$$(\Delta Q_{\text{net}})^2 = (\Delta Q_{\text{LH}})^2 + (\Delta Q_{\text{SH}})^2 + (\Delta Q_{\text{LW}})^2 + (\Delta Q_{\text{SW}})^2, \tag{A7}$$

with $\Delta Q_{\text{LH}} = 5\ \text{W m}^{-2}$, $\Delta Q_{\text{SH}} = 1.5\ \text{W m}^{-2}$, $\Delta Q_{\text{LW}} = 3.9\ \text{W m}^{-2}$, and $\Delta Q_{\text{SW}} = 5\ \text{W m}^{-2}$ (Colbo and Weller 2009). The error of the shortwave penetration term in Eq. (25) was calculated as

$$\begin{aligned}\left[\Delta\left(\frac{Q_{\text{pen}}}{\rho_0 c_p h_m}\right)\right]^2 &= \left(\frac{Q_{\text{pen}}}{\rho_0 c_p h_m}\,\frac{\Delta h_m}{h_m}\right)^2 + \left\{\frac{\Delta Q_{\text{SW}}}{\rho_0 c_p h_m}\left[R\exp\frac{-h_m}{\gamma_1} + (1-R)R\exp\frac{-h_m}{\gamma_2}\right]\right\}^2\\ &\quad + \left[\frac{Q_{\text{SW}}}{\rho_0 c_p}\frac{\Delta h_m}{h_m}\left(\frac{R}{\gamma_1}\exp\frac{-h_m}{\gamma_1} + \frac{1-R}{\gamma_2}\exp\frac{-h_m}{\gamma_2}\right)\right]^2 + \left\{\frac{Q_{\text{SW}}}{\rho_0 c_p}\left[R\exp\frac{-h_m}{\gamma_1}\Delta\left(\frac{1}{\gamma_1}\right)\right]\right\}^2,\\ &\quad + \left\{\frac{Q_{\text{SW}}}{\rho_0 c_p}\left[(1-R)\exp\frac{-h_m}{\gamma_2}\,\Delta\left(\frac{1}{\gamma_2}\right)\right]\right\}^2 + \left[\frac{Q_{\text{SW}}}{\rho_0 c_p h_m}\left(\exp\frac{-h_m}{\gamma_1} - \exp\frac{-h_m}{\gamma_2}\right)\Delta\,\frac{1}{2}R\right]^2\end{aligned} \tag{A8}$$

where $\Delta(1/\gamma_1) = 1.7\ \text{m}^{-1}$ (60%), $\Delta(1/\gamma_2) = 0.03\ \text{m}^{-1}$ (60%), and $\Delta R = 0.145$ (25%) (Farrar 2007).

The error of the evaporation term and the precipitation term in Eq. (24) was calculated as

$$\left[\Delta\left(\frac{ES_0}{h_m}\right)\right]^2 = \left(\frac{ES_0}{h_m}\,\frac{\Delta h_m}{h_m}\right)^2 + \left(\frac{\Delta ES_0}{h_m}\right)^2 + \left(\frac{E\Delta S_0}{h_m}\right)^2, \text{ and} \tag{A9}$$

$$\left[\Delta\left(\frac{PS_0}{h_m}\right)\right]^2 = \left(\frac{PS_0}{h_m}\,\frac{\Delta h_m}{h_m}\right)^2 + \left(\frac{\Delta PS_0}{h_m}\right)^2 + \left(\frac{P\Delta S_0}{h_m}\right)^2, \tag{A10}$$

respectively, where ΔE was estimated based on ΔQ_{LH} and $\Delta S_0 = 0.03$ and $\Delta P = 0.27\ \text{mm day}^{-1}$ were applied for both the WHOI and PICOSP moorings (Colbo and Weller 2009).

The error of the Ekman advection term of the MLS budget in Eq. (24) was calculated as

$$\begin{aligned}[\Delta(\mathbf{u}_{\text{Ek}}\cdot\nabla S_m)]^2 &= \left[\Delta\left(u_{\text{Ek}}\frac{\partial S_m}{\partial x}\right)\right]^2 + \left[\Delta\left(\upsilon_{\text{Ek}}\frac{\partial S_m}{\partial y}\right)\right]^2\\ &= \left(\Delta u_{\text{Ek}}\frac{\partial S_m}{\partial x}\right)^2 + \left[u_{\text{Ek}}\Delta\left(\frac{\partial S_m}{\partial x}\right)\right]^2\\ &\quad + \left(\Delta\upsilon_{\text{Ek}}\frac{\partial S_m}{\partial y}\right)^2 + \left[\upsilon_{\text{Ek}}\Delta\left(\frac{\partial S_m}{\partial y}\right)\right]^2.\end{aligned} \tag{A11}$$

Similarly, the error of the Ekman advection term of the MLT budget in Eq. (25) can be calculated as

$$\begin{aligned}[\Delta(\mathbf{u}_{\text{Ek}}\cdot\nabla T)]^2 &= \left(\Delta u_{\text{Ek}}\frac{\partial T}{\partial x}\right)^2 + \left[u_{\text{Ek}}\Delta\left(\frac{\partial T}{\partial x}\right)\right]^2 + \left(\Delta\upsilon_{\text{Ek}}\frac{\partial T}{\partial y}\right)^2\\ &\quad + \left[\upsilon_{\text{Ek}}\Delta\left(\frac{\partial T}{\partial y}\right)\right]^2.\end{aligned} \tag{A12}$$

The $\Delta(\partial S_m/\partial x)$ and $\Delta(\partial S_m/\partial y)$ in Eq. (A11) were estimated from the error of SSS from SMAP based on the additive propagation of error. The $\Delta(\partial T_m/\partial x)$ and $\Delta(\partial T_m/\partial y)$ in Eq. (A12) were estimated from the error of SST from OISST based on the additive propagation of error. The geostrophic advection term in Eqs. (24) and (25) were calculated in an analogous approach to Eqs. (A11) and (A12), respectively.

For the WHOI mooring, the error of Ekman velocity can be written as

$$(\Delta u_{\text{Ek}})^2 = \left(\frac{\Delta\tau^y_{\text{eff}}}{\rho_0 f h_m}\right)^2 + \left(\frac{\tau^y_{\text{eff}}}{\rho_0 f h_m}\,\frac{\Delta h_m}{h_m}\right)^2, \text{ and} \tag{A13}$$

$$(\Delta\upsilon_{\text{Ek}})^2 = \left(\frac{\Delta\tau^x_{\text{eff}}}{\rho_0 f h_m}\right)^2 + \left(\frac{\tau^x_{\text{eff}}}{\rho_0 f h_m}\,\frac{\Delta h_m}{h_m}\right)^2. \tag{A14}$$

The error of the effective wind stress was estimated as

$$(\Delta\tau^x_{\text{eff}})^2 = (\Delta\tau^x_0)^2 + (\Delta\tau^x_p)^2, \text{ and} \tag{A15}$$

$$(\Delta\tau^y_{\text{eff}})^2 = (\Delta\tau^y_0)^2 + (\Delta\tau^y_p)^2 \tag{A16}$$

where $\Delta\tau^x_0 = \Delta\tau^y_0 = 0.007\ \text{N m}^{-2}$ (Colbo and Weller 2009). The error of the surface geostrophic stress was estimated as

$$(\Delta\tau^x_p)^2 = \left(\frac{g}{f}\,\frac{\partial\rho}{\partial y}\,\Delta\nu\right)^2 + \left[\frac{g\nu}{f}\,\Delta\left(\frac{\partial\rho}{\partial y}\right)\right]^2, \text{ and} \tag{A17}$$

$$(\Delta\tau^y_p)^2 = \left(\frac{g}{f}\,\frac{\partial\rho}{\partial x}\,\Delta\nu\right)^2 + \left[\frac{g\nu}{f}\,\Delta\left(\frac{\partial\rho}{\partial x}\right)\right]^2, \tag{A18}$$

where $\Delta(\partial\rho/\partial x)$ and $\Delta(\partial\rho/\partial y)$ were estimated based on

$$(\Delta\rho)^2 = \left(\frac{\partial\rho}{\partial T}\,\Delta T\right)^2 + \left(\frac{\partial\rho}{\partial T}\,\Delta S\right)^2. \tag{A19}$$

The error of the eddy viscosity was estimated as the 95% confidence interval for the daily average of eddy viscosity, that is,

$$\Delta\nu = \frac{1.96 \times \mathrm{STD}(\nu)}{\sqrt{N}}, \tag{A20}$$

where $\mathrm{STD}(\nu)$ is the standard deviation of ν. The $\Delta\mathbf{u}_g$ at the WHOI mooring was estimated from $\Delta\mathbf{u}_m$ and $\Delta\mathbf{u}_{\mathrm{Ek}}$ based on the propagation of error.

For the PICOSP mooring, the error of the Ekman velocity was estimated as

$$(\Delta u_{\mathrm{Ek}})^2 = (\Delta u_g)^2 + (\Delta u)^2, \text{ and} \tag{A21}$$

$$(\Delta v_{\mathrm{Ek}})^2 = (\Delta v_g)^2 + (\Delta v)^2. \tag{A22}$$

Here, $\Delta\mathbf{u}_g$ at the PICOSP moorings was estimated based on the error of propagation from the SSH error of CMEMS. For the error of the Ekman current velocity derived from the OSCAR product, we applied $\Delta u = 0.1$ m s^{-1} and $\Delta v = 0.08$ m s^{-1}, which are the root-mean-square difference from drifter velocities in the region (150°–100°W, 10°N) (Johnson et al. 2007).

For the error estimation of the vertical diffusion term (Figs. 6b, 7b, 8b, 9b, 10b, and 11b), vertical diffusivity limits of 1×10^{-6} m^2 s^{-1} and 1×10^{-4} m^2 s^{-1} were applied to Eqs. (24) and (25). The upper limit of $\kappa_v = 1 \times 10^{-4}$ m^2 s^{-1} corresponds to the order of the turbulence diffusivity at the mixed layer base. For the error estimation of the sum of the forcing terms (Figs. 6a, 7a, 8a, 9a, 10a, and 11a), we used the difference between the vertical diffusion term ($\kappa_v = 2 \times 10^{-5}$ m^2 s^{-1}) and the larger limit of the error bar ($\kappa_v = 1 \times 10^{-4}$ m^2 s^{-1}).

For the estimation of the entrainment term, using Eqs. (6) and (22), Eq. (21) was transformed into

$$\begin{aligned} T_{\mathrm{ent}} &= \frac{1}{\Delta t}\left\{\frac{1}{h_m(t+\Delta t)}\left[\int_{-h_m(t+\Delta t)}^{0}\theta(z)dz - \int_{-h_m(t)}^{0}\theta(z)dz\right] - DT_m(t)\right\} \\ &= \frac{1}{\Delta t}\left\{\frac{1}{h_m(t+\Delta t)}\int_{-h_m(t+\Delta t)}^{0}\theta(z)dz - T_m(t)\right\}. \end{aligned} \tag{A23}$$

Thus, the error of the entrainment term can be written as

$$(\Delta T_{\mathrm{ent}})^2 = \frac{1}{\Delta t}\left(\left\{\Delta\left[\frac{1}{h_m(t+\Delta t)}\int_{-h_m(t+\Delta t)}^{0}\theta(z)dz\right]\right\}^2 + (\Delta T_m)^2\right). \tag{A24}$$

The first term on the right-hand side of Eq. (A24) was estimated similar to ΔT_m [Eq. (A1)] and ΔS_{ent} was estimated in an analogous way to Eq. (A24).

APPENDIX B

Residuals of the Mixed Layer Salinity and Temperature Budgets

In sections 3b and 3c, we constructed the MLS and MLT budgets to investigate the formation mechanism of BLs and TIs, respectively. Although the sum of the forcing terms showed a relatively good agreement with the MLS and MLT tendency at the SPURS-2 moorings, some mismatch occurred as a result of missing terms in the budget [R_S and R_T in Eqs. (24) and (25)]. For example, the eddy component of horizontal advection ($-\mathbf{u}_m \cdot \nabla T'_m$ and $-\mathbf{u}_m \cdot \nabla S'_m$) and the eddy flux [term 7 in Eqs. (4) and (5)] are not accounted for in the budget. In addition, we only consider the effect of deepening and shoaling of the mixed layer in the calculation of the entrainment terms [term 1 in Eqs. (18) and (19)] using Eqs. (21)–(23), and the effects of lateral induction and Ekman upwelling/downwelling on the entrainment [terms 2 and 3 in Eqs. (18) and (19)] were not included. The residual terms R_S and R_T of the MLS and MLT budget, respectively, can be expressed as

$$\begin{aligned} R_S = &-\mathbf{u}_m \cdot \nabla S'_m - \frac{(S_m - S_{-h})}{h_m}(\mathbf{u}_{-h} \cdot \nabla h_m + w_{-h}) \\ &- \frac{1}{h_m}\nabla \cdot \int_{-h_m}^{0} \hat{\mathbf{u}}\hat{S}\,dz, \text{ and} \end{aligned} \tag{B1}$$

$$\begin{aligned} R_T = &-\mathbf{u}_m \cdot \nabla T'_m - \frac{(T_m - T_{-h})}{h_m}(\mathbf{u}_{-h} \cdot \nabla h_m + w_{-h}) \\ &- \frac{1}{h_m}\nabla \cdot \int_{-h_m}^{0} \hat{\mathbf{u}}\hat{\theta}\,dz. \end{aligned} \tag{B2}$$

The eddy component of the horizontal advection is assumed to be driven by horizontal diffusion in applying the following parameterization,

$$-\mathbf{u}_m \cdot \nabla S'_m = -\kappa_h \nabla^2 S_m, \text{ and} \tag{B3}$$

$$-\mathbf{u}_m \cdot \nabla T'_m = -\kappa_h \nabla^2 T_m, \tag{B4}$$

where κ_h is horizontal diffusivity. The vertical velocity at the MLD, w_{-h}, is assumed to be driven by the convergence and divergence of the horizontal transport of the effective wind stress (e.g., Yu 2011; Cronin and Tozuka 2016; Katsura et al. 2020),

$$w_{-h} = \nabla\left(\frac{\tau^y_{\mathrm{eff}}}{\rho_0 f}, -\frac{\tau^x_{\mathrm{eff}}}{\rho_0 f}\right) = \frac{\nabla \times \tau_{\mathrm{eff}}}{\rho_0 f} + \frac{\tau^x_{\mathrm{eff}}}{\rho_0 f^2}\frac{\partial f}{\partial y}. \tag{B5}$$

We are unable to accurately estimate the horizontal gradient of the MLD (i.e., ∇h_m) and the vertical profile of horizontal velocity (i.e., $\nabla \cdot \int_{-h_m}^{0} \hat{\mathbf{u}}\hat{\theta}\,dz$ and $\nabla \cdot \int_{-h_m}^{0} \hat{\mathbf{u}}\hat{S}\,dz$) from the SPURS-2 mooring datasets and so lateral induction and eddy flux will be part of the unresolved residual [i.e., left-hand side of Eqs. (B1) and (B2)]. The contribution of horizontal diffusion and Ekman upwelling was estimated and compared to R_S in Eq. (24) and R_T in Eq. (25). A horizontal diffusivity κ_h of 8×10^3 m^2 s^{-1} is appropriate at the SPURS-2 mooring sites (Zhurbas and Oh 2004). Finally, to estimate w_{-h}, the effective wind stress [Eq. (12)] was estimated from CCMP wind using the COARE 3.5 algorithm and using the eddy viscosity [Eq. (14)] determined for the WHOI mooring.

TABLE B1. Correlations of the MLS ($\partial S_m/\partial t$) and MLT ($\partial T_m/\partial t$) tendencies with the sum of the forcing terms (FT) on the right-hand side of Eqs. (24) and (25), respectively, and the residual terms (R_S and R_T). Bold numbers indicate significant values at the 95% confidence level that are given by $R = 0.53$ for the WHOI and PICOSP02 moorings and $R = 0.63$ for the PICOSP01 mooring. Values in parentheses indicate the root-mean-square differences. These statistics were calculated for the 31-day moving-averaged time series.

	WHOI		PICOSP01		PICOSP02	
	$\partial S_m/\partial t$	$\partial T_m/\partial t$	$\partial S_m/\partial t$	$\partial T_m/\partial t$	$\partial S_m/\partial t$	$\partial T_m/\partial t$
FT	0.42 (0.013)	**0.56** (0.017)	**0.66** (0.010)	**0.75** (0.017)	**0.57** (0.011)	0.39 (0.022)
R_S	**0.72** (0.009)	—	0.34 (0.013)	—	0.43 (0.012)	—
R_T	—	0.24 (0.019)	—	−0.16 (0.025)	—	0.18 (0.024)

Correlations and root-mean-square differences of the 31-day moving-averaged MLS and MLT tendency [left-hand side of Eqs. (24) and (25)] with the sum of forcing terms [right-hand side of Eqs. (24) and (25)] and the residual terms are given in Table B1. Here, the sample number (N) for the significance of the correlations was estimated by dividing the length of the time series (T) by 31 days ($N = 14$ for the WHOI mooring where $T = 438$ days, $N = 10$ for the PICOSP01 mooring where $T = 312$ days, and $N = 14$ for the PICOSP02 mooring where $T = 437$ days). The MLS and MLT tendencies showed higher and significant correlations and smaller root-mean-square difference with the sum of the forcing terms than with the residual terms except for the MLS budget at the WHOI mooring. These statistics imply that the constructed MLS and MLT budget better explain the MLS variability at the PICOSP moorings and MLT variability at the three SPURS-2 moorings than the residual terms although the residual terms were not negligible.

For the MLS budget, neither Ekman upwelling nor horizontal diffusion were found to be balanced by the residual term at the SPURS-2 moorings (Fig. B1). The effective

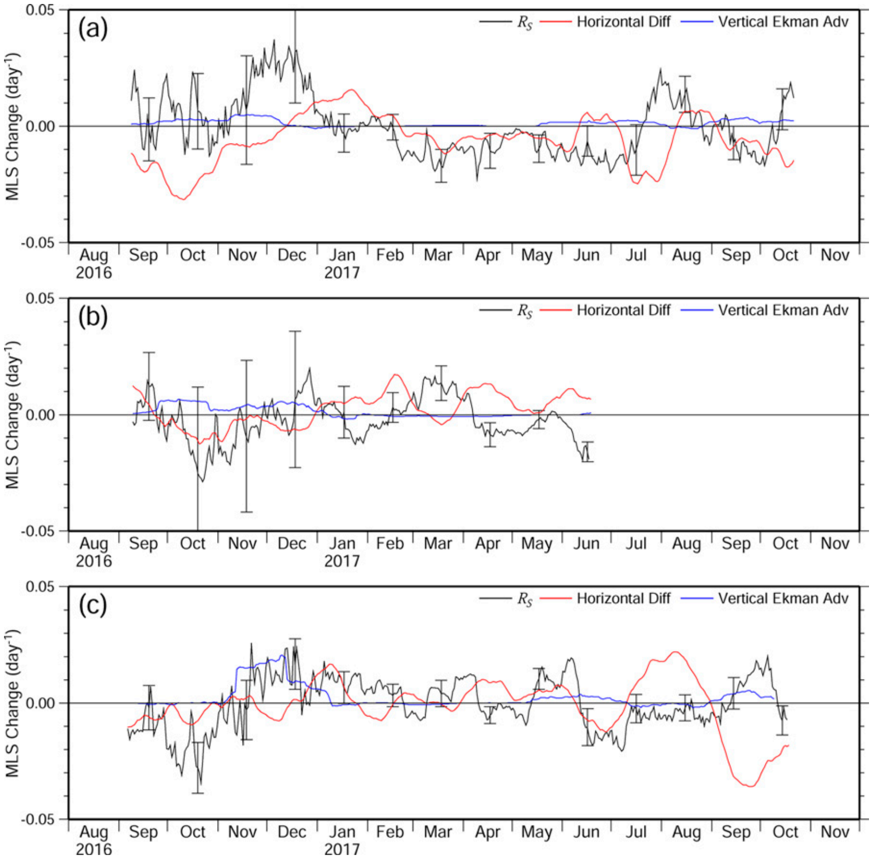

FIG. B1. Time series of 31-day moving-averaged MLS budget residual R_S (day^{-1}; black), horizontal diffusion (red), and entrainment by Ekman upwelling (blue) at the (a) WHOI mooring, (b) PICOSP01 mooring, and (c) PICOSP02 mooring.

TABLE B2. Correlations of R_S and R_T with horizontal diffusion and Ekman upwelling. Values in parentheses indicate the root-mean-square differences. These statistics were calculated for the 31-day moving-averaged time series. None of correlations are significant at the 95% confidence level given by $R = 0.53$ for the WHOI mooring, $R = 0.63$ for the PICOSP01 mooring, and $R = 0.55$ for the PICOSP02 mooring. The sample number (N) for the estimation of the significance was the same as in Table B1, but $N = 14$ for the PICOSP02 mooring due to the short period of air–sea flux measurements used for the estimation of w_{-h}.

	WHOI		PICOSP01		PICOSP02	
	R_S	R_T	R_S	R_T	R_S	R_T
Ekman upwelling	0.18 (0.013)	0.47 (0.016)	−0.23 (0.011)	0.40 (0.017)	0.40 (0.011)	0.29 (0.021)
Horizontal diffusion	−0.07 (0.018)	0.13 (0.018)	0.13 (0.012)	0.50 (0.017)	−0.05 (0.017)	−0.48 (0.028)

wind stress curl and w_{-h} were positive (i.e., Ekman upwelling) almost throughout the whole observation period. Since S_{-h} was saltier than the MLS, as salinity increased with depth at the SPURS-2 moorings (Figs. 3a, 4a, and 5a), Ekman upwelling acted to increase the MLS (Fig. B1). For the WHOI and PICOSP01 mooring, the amplitude of the Ekman upwelling term was smaller than that of the residual term (Figs. B1a,b), and these two terms showed no significant correlation (Table B2). At the PICOSP02 mooring, although the Ekman upwelling term showed a comparable amplitude to the residual term such as in November–December 2016, the correlation was not significant at 95% confidence. The horizontal diffusion term [Eq. (B3)] showed little agreement in amplitude or phase and low correlation with the residual of the MLS budget at all of the SPURS-2 moorings (Fig. B1; Table B2).

For the MLT budget, the variation of the residual did not show an agreement with neither horizontal diffusion nor Ekman upwelling at the SPURS-2 moorings (Fig. B2). The amplitude of the Ekman upwelling term was smaller than that of the residual, as also found in the MLS budget at the SPURS-2 moorings (Fig. B2). Although the Ekman upwelling showed a positive correlation with the residual term, the correlation was not significant at 95% confidence (Table B2).

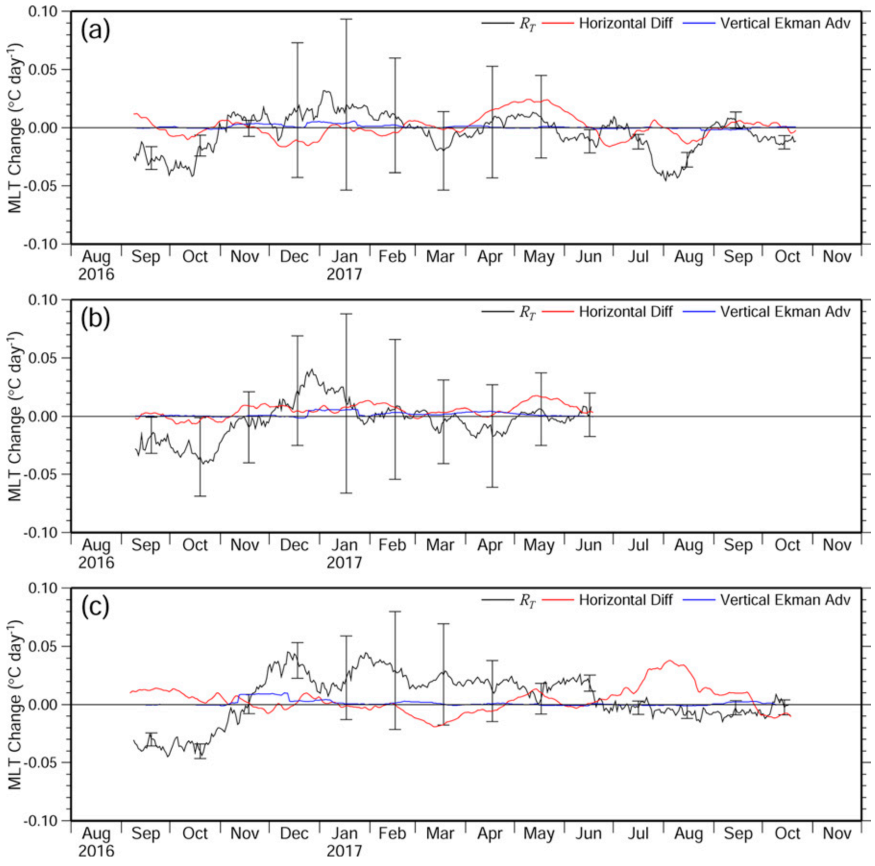

FIG. B2. Time series of 31-day moving-averaged MLT budget residual R_T (°C day^{-1}; black), horizontal diffusion (red), and entrainment by Ekman upwelling (blue) at the (a) WHOI mooring, (b) PICOSP01 mooring, and (c) PICOSP02 mooring.

Thus, the residual of the MLT budget was not attributable to the Ekman upwelling. As with the MLS budget, there was little agreement and no significant correlation of the horizontal diffusion amplitude and phase [Eq. (B4)] with the MLT residual at any of the SPURS-2 moorings (Fig. B2; Table B2).

For the MLS budget, although some of the residual at the PICOSP02 mooring was potentially explained by Ekman pumping, the MLS residual during other periods at the PICOSP02 mooring, and for the entire period at the WHOI and PICOSP01 moorings, was not attributable to neither Ekman pumping nor horizontal diffusion (Table B2; Fig. B1). In particular, for the WHOI mooring neither Ekman upwelling nor horizontal diffusion were correlated with the residual terms (Table B2). Furthermore, there was a large discrepancy between the MLS tendency and the sum of the forcing terms (Table B1; Figs. 6a and B1a) while the residual term was significantly correlated with the tendency (Table B1). The MLT residual at the three SPURS-2 moorings was also not explainable by Ekman pumping nor horizontal diffusion or at least they were not significantly correlated with the residual term of the budgets (Table B2; Fig. B2). These results suggested that the residual terms of the MLS and MLT budgets at the SPURS-2 moorings are also partially due to the missing lateral induction term, the eddy flux term, and/or the error associated with each forcing term and, in particular, these missing processes likely significantly contributed the MLS budget at the WHOI mooring. Nonetheless, the error bars of the residual terms mostly overlapped with zero (Figs. B1 and B2), suggesting that the residual of the MLS and MLT budget are potentially explained by the error associated with the forcing terms. Although unsatisfactory, it is difficult to further pursue the cause of the residual terms in the MLS and MLT budget with our available dataset.

REFERENCES

Akima, H., 1970: A new method of interpolation and smooth curve fitting based on local procedures. *J. Assoc. Comput. Mach.*, **17**, 589–602, https://doi.org/10.1145/321607.321609.

Alory, G., C. Maes, T. Delcroix, N. Reul, and S. Ilig, 2012: Seasonal dynamics of sea surface salinity off Panama: The far eastern Pacific fresh pool. *J. Geophys. Res.*, **117**, C04028, https://doi.org/10.1029/2011JC007802.

Balaguru, K., P. Chang, R. Saravanan, L. R. Leung, Z. Xu, M. K. Li, and J. S. Hsieh, 2012: Ocean barrier layers' effect on tropical cyclone intensification. *Proc. Natl. Acad. Sci. USA*, **109**, 14 343–14 347, https://doi.org/10.1073/pnas.1201364109.

Bingham, F. M., G. R. Foltz, and M. J. McPhaden, 2010: Seasonal cycles of surface layer salinity in the Pacific Ocean. *Ocean Sci.*, **6**, 775–787, https://doi.org/10.5194/os-6-775-2010.

Bonjean, F., and G. S. Lagerloef, 2002: Diagnostic model and analysis of the surface currents in the tropical Pacific Ocean. *J. Phys. Oceanogr.*, **32**, 2938–2954, https://doi.org/10.1175/1520-0485(2002)032<2938:DMAAOT>2.0.CO;2.

Chi, N.-H., R.-C. Lien, and E. A. D'Asaro, 2021: The mixed layer salinity budget in the central equatorial Indian Ocean. *J. Geophys. Res. Oceans*, **126**, e2021JC017280, https://doi.org/10.1029/2021JC017280.

Colbo, K., and R. A. Weller, 2009: Accuracy of the IMET sensor package in the subtropics. *J. Atmos. Oceanic Technol.*, **26**, 1867–1890, https://doi.org/10.1175/2009JTECHO667.1.

Cronin, M. F., and M. J. McPhaden, 2002: Barrier layer formation during westerly wind bursts. *J. Geophys. Res.*, **107**, 8020, https://doi.org/10.1029/2001JC001171.

——, and W. S. Kessler, 2009: Near-surface shear flow in the tropical Pacific cold tongue front. *J. Phys. Oceanogr.*, **39**, 1200–1215, https://doi.org/10.1175/2008JPO4064.1.

——, and T. Tozuka, 2016: Near-surface shear flow in the tropical Pacific cold tongue front. *Sci. Rep.*, **9**, 28842, https://doi.org/10.1038/srep28842.

——, and Coauthors, 2013: Formation and erosion of the seasonal thermocline in the Kuroshio Extension Recirculation Gyre. *Deep-Sea Res. II*, **85**, 62–74, https://doi.org/10.1016/j.dsr2.2012.07.018.

——, N. A. Pelland, S. R. Emerson, and W. R. Crawford, 2015: Estimating diffusivity from the mixed layer heat and salt balances in the North Pacific. *J. Geophys. Res. Oceans*, **120**, 7346–7362, https://doi.org/10.1002/2015JC011010.

de Boyer Montégut, C., J. Mignot, A. Lazar, and S. Cravatte, 2007: Control of salinity on the mixed layer depth in the World Ocean: 1. General description. *J. Geophys. Res.*, **112**, C06011, https://doi.org/10.1029/2006JC003953.

Delcroix, T., A. Chaigneau, D. Soviadan, J. Boutin, and C. Pegliasco, 2019: Eddy-induced salinity changes in the tropical Pacific. *J. Geophys. Res. Oceans*, **124**, 374–389, https://doi.org/10.1029/2018JC014394.

Dong, S., S. T. Gille, and J. Sprintall, 2007: An assessment of the Southern Ocean mixed layer heat budget. *J. Climate*, **20**, 4425–4442, https://doi.org/10.1175/JCLI4259.1.

Drushka, K., J. Sprintall, and S. T. Gille, 2014: Subseasonal variations in salinity and barrier-layer thickness in the eastern equatorial Indian Ocean. *J. Geophys. Res. Oceans*, **119**, 805–823, https://doi.org/10.1002/2013JC009422.

Edson, J. B., and Coauthors, 2013: On the exchange of momentum over the open ocean. *J. Phys. Oceanogr.*, **43**, 1589–1610, https://doi.org/10.1175/JPO-D-12-0173.1.

Fairall, C. W., E. F. Bradley, J. S. Godfrey, G. A. Wick, J. B. Edson, and G. S. Young, 1996: Cool-skin and warm-layer effects on sea surface temperature. *J. Geophys. Res.*, **101**, 1295–1308, https://doi.org/10.1029/95JC03190.

——, ——, J. E. Hare, A. A. Grachev, and J. B. Edson, 2003: Bulk parameterization of air–sea fluxes: Updates and verification for the COARE algorithm. *J. Climate*, **16**, 571–591, https://doi.org/10.1175/1520-0442(2003)016<0571:BPOASF>2.0.CO;2.

Farrar, J. T., 2007: Air-sea interaction at contrasting sites in the eastern tropical Pacific: Mesoscale variability and atmospheric convection at 10°N. PhD thesis, Massachusetts Institute of Technology, 66 pp.

——, and R. A. Weller, 2006: Intraseasonal variability near 10°N in the eastern tropical Pacific Ocean. *J. Geophys. Res.*, **111**, C05015, https://doi.org/10.1029/2005JC002989.

——, and A. J. Plueddemann, 2019: On the factors driving upper-ocean salinity variability at the western edge of the eastern Pacific fresh pool. *Oceanography*, **32**, 30–39, https://doi.org/10.5670/oceanog.2019.209.

——, and Coauthors, 2015: Salinity and temperature balances at the SPURS central mooring during fall and winter. *Oceanography*, **28**, 56–65, https://doi.org/10.5670/oceanog.2015.06.

Foltz, G. R., and M. J. McPhaden, 2005: Mixed layer heat balance on intraseasonal time scales in the northwestern tropical

Atlantic Ocean. *J. Climate*, **18**, 4168–4184, https://doi.org/10.1175/JCLI3531.1.

——, and ——, 2009: Impact of barrier layer thickness on SST in the central tropical North Atlantic. *J. Climate*, **22**, 285–299, https://doi.org/10.1175/2008JCLI2308.1.

——, S. A. Grodsky, J. A. Carton, and M. J. McPhaden, 2003: Seasonal mixed layer heat budget of the tropical Atlantic Ocean. *J. Geophys. Res.*, **108**, 3146, https://doi.org/10.1029/2002JC001584.

——, ——, ——, and ——, 2004: Seasonal salt budget of the northwestern tropical Atlantic Ocean along 38°W. *J. Geophys. Res.*, **109**, C03052, https://doi.org/10.1029/2003JC002111.

Girishkumar, M. S., J. Joseph, V. P. Thangaprakash, P. Vijay, and M. J. McPhaden, 2017: Mixed layer temperature budget for the northward propagating summer Monsoon Intraseasonal Oscillation (MISO) in the central Bay of Bengal. *J. Geophys. Res. Oceans*, **122**, 8841–8854, https://doi.org/10.1002/2017JC013073.

Godfrey, J. S., and E. J. Lindstrom, 1989: The heat budget of the equatorial western Pacific surface mixed layer. *J. Geophys. Res.*, **94**, 8007–8017, https://doi.org/10.1029/JC094iC06p08007.

Guimbard, S., N. Reul, B. Chapron, M. Umbert, and C. Maes, 2017: Seasonal and interannual variability of the eastern tropical Pacific Fresh Pool. *J. Geophys. Res. Oceans*, **122**, 1749–1771, https://doi.org/10.1002/2016JC012130.

Hasson, A., J. T. Farrar, J. Boutin, F. Bingham, and T. Lee, 2019: Intraseasonal variability of surface salinity in the eastern tropical Pacific associated with mesoscale eddies. *J. Geophys. Res. Oceans*, **124**, 2861–2875, https://doi.org/10.1029/2018JC014175.

Hsin, Y. C., and B. Qiu, 2012: Seasonal fluctuations of the surface North Equatorial Countercurrent (NECC) across the Pacific basin. *J. Geophys. Res.*, **117**, C06001, https://doi.org/10.1029/2011JC007794.

Jerlov, N. G., 1976: *Marine Optics*. 2nd ed. Elsevier Oceanography Series, Vol. 14, Elsevier, 230 pp.

Jin, F.-F., J. Boucharel, and I.-I. Lin, 2014: Eastern Pacific tropical cyclone intensified by El Niño delivery of subsurface ocean heat. *Nature*, **516**, 82–85, https://doi.org/10.1038/nature13958.

Johnson, E. S., F. Bonjean, G. S. E. Lagerloef, J. T. Gunn, and G. T. Mitchum, 2007: Validation and error analysis of OSCAR sea surface currents. *J. Atmos. Oceanic Technol.*, **24**, 688–701, https://doi.org/10.1175/JTECH1971.1.

Katsura, S., and J. Sprintall, 2020: Seasonality and formation of barrier layers and associated temperature inversions in the eastern tropical North Pacific. *J. Phys. Oceanogr.*, **50**, 791–808, https://doi.org/10.1175/JPO-D-19-0194.1.

——, E. Oka, B. Qiu, and N. Schneider, 2013: Formation and subduction of North Pacific tropical water and their interannual variability. *J. Phys. Oceanogr.*, **43**, 2400–2415, https://doi.org/10.1175/JPO-D-13-031.1.

——, H. Ueno, H. Mitsudera, and S. Kouketsu, 2020: Spatial distribution and seasonality of halocline structures in the subarctic North Pacific. *J. Phys. Oceanogr.*, **50**, 95–109. https://doi.org/10.1175/JPO-D-19-0133.1

——, J. Sprintall, and F. M. Bingham, 2021: Upper ocean stratification in the eastern Pacific during the SPURS-2 field campaign. *J. Geophys. Res. Oceans*, **126**, e2020JC016591, https://doi.org/10.1029/2020JC016591.

Kim, S.-B., I. Fukumori, and T. Lee, 2006: The closure of the ocean mixed layer temperature budget using level-coordinate model fields. *J. Atmos. Oceanic Technol.*, **23**, 840–853, https://doi.org/10.1175/JTECH1883.1.

Kummerow, C., 1998: Beamfilling errors in passive microwave rainfall retrievals. *J. Appl. Meteor.*, **37**, 356–370, https://doi.org/10.1175/1520-0450(1998)037<0356:BEIPMR>2.0.CO;2.

Lee, T., G. Lagerloef, M. M. Gierach, H.-Y. Kao, S. Yueh, and K. Dohan, 2012: Aquarius reveals salinity structure of tropical instability waves. *Geophys. Res. Lett.*, **39**, L12610, https://doi.org/10.1029/2012GL052232.

Lindstrom, E. J., J. B. Edson, J. J. Schanze, and A. Y. Shcherbina, 2019: SPURS-2: Salinity processes in the upper-ocean regional study 2. The eastern equatorial Pacific experiment. *Oceanography*, **32**, 15–19, https://doi.org/10.5670/oceanog.2019.207.

Liu, X., and H. Zhou, 2020: Seasonal variations of the North Equatorial Current across the Pacific Ocean. *J. Geophys. Res. Oceans*, **125**, e2019JC015895, https://doi.org/10.1029/2019JC015895.

Lukas, R., and E. Lindstrom, 1991: The mixed layer of the western equatorial Pacific Ocean. *J. Geophys. Res.*, **96**, 3343–3357, https://doi.org/10.1029/90JC01951.

Masson, S., J.-P. Boulanger, C. Menkes, P. Delecluse, and T. Yamagata, 2004: Impact of salinity on the 1997 Indian Ocean dipole event in a numerical experiment. *J. Geophys. Res.*, **109**, C02002, https://doi.org/10.1029/2003JC001807.

Meissner, T., and F. J. Wentz, 2019: SMAP sea surface salinity products, ver. 4.0. PO.DAAC, accessed 21 May 2020, https://doi.org/10.5067/SMP40-3SPCS.

Mickett, J. B., Y. L. Serra, M. F. Cronin, and M. H. Alford, 2010: Resonant forcing of mixed layer inertial motions by atmospheric easterly waves in the northeastern tropical Pacific. *J. Phys. Oceanogr.*, **40**, 401–416, https://doi.org/10.1175/2009JPO4276.1.

Moisan, J. R., and P. P. Niiler, 1998: The seasonal heat budget of the North Pacific: Net heat flux and heat storage rates (1950–1990). *J. Phys. Oceanogr.*, **28**, 401–421, https://doi.org/10.1175/1520-0485(1998)028<0401:TSHBOT>2.0.CO;2.

Osse, J., S. Stalin, C. Meinig, and H. Milburn, 2015: The PRAWLER, a vertical profiler: Powered by wave energy. *Oceans 2015 MTS/IEEE*, IEEE, Washington, D.C., 1–8, https://doi.org/10.23919/OCEANS.2015.7404354.

Paulson, C. A., and J. J. Simpson, 1977: Irradiance measurements in the upper ocean. *J. Phys. Oceanogr.*, **7**, 952–956, https://doi.org/10.1175/1520-0485(1977)007<0952:IMITUO>2.0.CO;2.

Pujiana, K., and M. J. McPhaden, 2018: Ocean surface layer response to convectively coupled Kelvin waves in the eastern equatorial Indian Ocean. *J. Geophys. Res. Oceans*, **123**, 5727–5741, https://doi.org/10.1029/2018JC013858.

Ren, L., and S. C. Riser, 2009: Seasonal salt budget in the northeast Pacific Ocean. *J. Geophys. Res.*, **114**, C12004, https://doi.org/10.1029/2009JC005307.

——, K. Speer, and E. P. Chassignet, 2011: The mixed layer salinity budget and sea ice in the Southern Ocean. *J. Geophys. Res.*, **116**, C08031, https://doi.org/10.1029/2010JC006634.

Reynolds, R. W., T. M. Smith, C. Liu, D. B. Chelton, K. S. Casey, and M. G. Schlax, 2007: Daily high-resolution blended analyses for sea surface temperature. *J. Climate*, **20**, 5473–5496, https://doi.org/10.1175/2007JCLI1824.1.

Roemmich, D., M. Morris, W. R. Young, and J. R. Donguy, 1994: Fresh equatorial jets. *J. Phys. Oceanogr.*, **24**, 540–558, https://doi.org/10.1175/1520-0485(1994)024<0540:FEJ>2.0.CO;2.

Saha, A., N. Serra, and D. Stammer, 2021: Growth and decay of northwestern tropical Atlantic barrier layers. *J. Geophys. Res. Oceans*, **126**, e2020JC016956, https://doi.org/10.1029/2020JC016956.

Sprintall, J., and M. Tomczak, 1992: Evidence of the barrier layer in the surface layer of the tropics. *J. Geophys. Res.*, **97**, 7305–7316, https://doi.org/10.1029/92JC00407.

Suga, T., K. Motoki, and Y. Aoki, 2004: The North Pacific climatology of winter mixed layer and mode waters. *J. Phys. Oceanogr.*, **34**, 3–22, https://doi.org/10.1175/1520-0485(2004)034<0003:TNPCOW>2.0.CO;2.

Veneziani, M., A. Griffa, Z. Garrafo, and J. A. Mensa, 2014: Barrier layers in the tropical South Atlantic: Mean dynamics and submesoscale effects. *J. Phys. Oceanogr.*, **44**, 265–288, https://doi.org/10.1175/JPO-D-13-064.1.

Vialard, J., and P. Delecluse, 1998a: An OGCM study for the TOGA decade. Part I: Role of salinity in the physics of the western Pacific fresh pool. *J. Phys. Oceanogr.*, **28**, 1071–1088, https://doi.org/10.1175/1520-0485(1998)028<1071:AOSFTT>2.0.CO;2.

——, and ——, 1998b: An OGCM study for the TOGA decade. Part II: Barrier-layer formation and variability. *J. Phys. Oceanogr.*, **28**, 1089–1106, https://doi.org/10.1175/1520-0485(1998)028<1089:AOSFTT>2.0.CO;2.

Wentz, F. J., J. Scott, R. Hoffman, M. Leidner, R. Atlas, and J. Ardizzone, 2015: Remote Sensing Systems Cross-Calibrated Multi-Platform (CCMP) 6-hourly ocean vector wind analysis product on 0.25 deg grid, version 2.0. Remote Sensing Systems, accessed 1 September 2020, http://www.remss.com/measurements/ccmp.

Wijesekera, H. W., D. L. Rudnick, C. A. Paulson, S. D. Pierce, W. S. Pegau, J. Mickett, and M. C. Gregg, 2005: Upper ocean heat and freshwater budgets in the eastern Pacific warm pool. *J. Geophys. Res.*, **110**, C08004, https://doi.org/10.1029/2004JC002511.

Xie, S.-P., and S. G. H. Philander, 1994: A coupled ocean–atmosphere model of relevance to the ITCZ in the eastern Pacific. *Tellus*, **46A**, 340–350, https://doi.org/10.3402/tellusa.v46i4.15484.

Yan, Y., L. Li, and C. Wang, 2017: The effects of oceanic barrier layer on the upper ocean response to tropical cyclones. *J. Geophys. Res. Oceans*, **122**, 4829–4844, https://doi.org/10.1002/2017JC012694.

Yin, X., J. Boutin, G. Reverdin, T. Lee, N. Martin, and S. Arnault, 2014: SMOS sea surface salinity signatures of tropical instability waves. *J. Geophys. Res. Oceans*, **119**, 7811–7826, https://doi.org/10.1002/2014JC009960.

Yu, L. S., 2011: A global relationship between the ocean water cycle and near-surface salinity. *J. Geophys. Res.*, **116**, C10025, https://doi.org/10.1029/2010JC006937.

Zhurbas, V., and I. S. Oh, 2004: Drifter-derived maps of lateral diffusivity in the Pacific and Atlantic Oceans in relation to surface circulation patterns. *J. Geophys. Res.*, **109**, C05015, https://doi.org/10.1029/2003JC002241.